

Structure of penetrable-rod fluids: Exact properties and comparison between Monte Carlo simulations and two analytic theories

Alexandr Malijevský*

*E. Hála Laboratory of Thermodynamics, Academy of Science of the Czech Republic,
Prague 6, Czech Republic and Institute of Theoretical Physics,
Faculty of Mathematics and Physics, Charles University, Prague 8, Czech Republic*

Andrés Santos†

Departamento de Física, Universidad de Extremadura, E-06071 Badajoz, Spain

(Dated: December 27, 2021)

Bounded potentials are good models to represent the effective two-body interaction in some colloidal systems, such as dilute solutions of polymer chains in good solvents. The simplest bounded potential is that of penetrable spheres, which takes a positive finite value if the two spheres are overlapped, being 0 otherwise. Even in the one-dimensional case, the penetrable-rod model is far from trivial, since interactions are not restricted to nearest neighbors and so its exact solution is not known. In this paper the structural properties of one-dimensional penetrable rods are studied. We first derive the exact correlation functions of penetrable-rod fluids to second order in density at any temperature, as well as in the high-temperature and zero-temperature limits at any density. It is seen that, in contrast to what is generally believed, the Percus–Yevick equation does not yield the exact cavity function in the hard-rod limit. Next, two simple analytic theories are constructed: a high-temperature approximation based on the exact asymptotic behavior in the limit $T \rightarrow \infty$ and a low-temperature approximation inspired by the exact result in the opposite limit $T \rightarrow 0$. Finally, we perform Monte Carlo simulations for a wide range of temperatures and densities to assess the validity of both theories. It is found that they complement each other quite well, exhibiting a good agreement with the simulation data within their respective domains of applicability and becoming practically equivalent on the borderline of those domains. A comparison with numerical solutions of the Percus–Yevick and the hypernetted-chain approximations is also carried out. Finally, a perspective on the extension of our two heuristic theories to the more realistic three-dimensional case is provided.

I. INTRODUCTION

In the last few years, the study of the structural and thermodynamic equilibrium properties of fluids with particles interacting via strongly repulsive potentials have experienced a noticeable revival because of their interest in the physics of some colloidal systems. For instance, the effective interaction between two sterically stabilized colloidal particles can be accurately modeled by the hard-sphere potential.¹

On the other hand, the effective two-body interaction in other colloidal systems is much softer. For instance, the interaction potential for star polymers in good solvents can be shown to be ultrasoft, diverging only logarithmically for short distances.^{1,2} Furthermore, in the case of dilute solutions of polymer chains in good solvents, the centers of mass of two polymer chains can be separated by a distance smaller than the sum of their respective radii of gyration (and even can coincide at the same point), without violation of the excluded-volume conditions.¹ In such a case, the effective two-body potential is a *bounded* one, being well represented by the Gaussian core model.^{3,4,5,6,7,8}

The simplest bounded potential is that of so-called penetrable spheres (PS), which is defined as

$$\varphi(r) = \begin{cases} \epsilon, & r < \sigma, \\ 0, & r > \sigma, \end{cases} \quad (1.1)$$

where $\epsilon > 0$. This interaction potential was suggested by Marquest and Witten⁹ as a simple theoretical approach to the explanation of the experimentally observed crystallization of copolymer mesophases. In the last few years, the PS model has been the subject of several studies.^{7,10,11,12,13,14,15,16,17,18,19} Density-functional theory^{11,12} predicts a freezing transition to fcc solid phases with multiply occupied lattice sites. The existence of clusters of overlapped particles (or “clumps”) in the PS crystal and glass was already pointed out by Klein et al.,¹⁰ who also performed Monte Carlo (MC) simulations on the system. In the fluid phase, the standard integral equation theories in general are not very reliable in describing the structure of the PS fluid, especially inside the core.¹¹ While the number of overlapped pairs is overestimated by the hypernetted-chain (HNC) theory, it is strongly underestimated by the Percus–Yevick (PY) theory. Other more sophisticated closures,^{13,17} as well as Rosenfeld’s fundamental-measure theory,¹⁴ are able to predict the correlations functions with a much higher precision. Only in the combined high-temperature, high-density limit is the PS model amenable to an exact analytical treatment.¹⁸ As applications of the model, let us mention that a mixture of colloids and non-interacting polymer coils, where the colloid-colloid interaction is assumed to be that of hard spheres and the colloid-polymer interaction is described by the PS model, has been studied.¹⁵ The inhomogeneous structure of penetrable

spheres in a spherical pore has also been investigated.¹⁶ In addition, some nonequilibrium properties have been analyzed recently¹⁹ and in the past.²⁰

As mentioned above, the classical integral equation theories (PY and HNC) do not describe satisfactorily well the structure of the PS fluid, especially inside the overlapping region, for the whole range of fluid densities and temperatures. Thus, the PS model provides a stringent benchmark to test alternative theories.^{13,14,17} Even in the one-dimensional (1D) case, the PS model is far from trivial, since interactions are not restricted to nearest neighbors and so its exact solution is not known. A surprising consequence of the boundedness of the PS potential in the 1D case is the plausible existence of a fluid-crystal phase transition,¹⁸ thus providing one of the rare examples of phase transitions in 1D systems.²¹

Statistical mechanics has a long tradition of studying 1D systems, especially in those cases where an exact solution to the many-body problem has been found.²² Of course, the 1D PS model does not intend to describe all the properties of real polymers in solution, for which spatial dimensionality is known to be important.²³ However, it seems worthwhile studying the 1D PS model in order to understand some of the subtleties of the PS interaction and also to serve as a playground to test theoretical approaches that can be extended to the more realistic 3D case.

The main aim of this work is to explore the possibility of constructing simple analytic theories for the structural properties of the 1D PS fluid, based on known behaviors in the extreme cases of high and zero temperatures. Before proposing those theories and in order to gain some insight, the exact properties in the limits of low density, high temperature, and zero temperature are worked out in Sec. II, some technical details being relegated to an Appendix. In particular, it is seen that the PY equation does not yield the exact hard-rod correlation functions for all distances, in contrast to what is generally believed.^{24,25} As a simple extension to finite temperatures of the mean-field solution (asymptotically exact in the combined limit where the reduced temperature and density go to infinity, its ratio being kept finite), we propose a high-temperature (HT) approximation in Sec. III. A subtler task consists of the extension to finite temperatures, imposing some basic continuity conditions, of the exact solution for hard rods. This is carried out in Sec. IV, resulting in what we call the low-temperature (LT) approximation. Both approximations are compared with our own MC simulations in Sec. V. It is observed that both theories complement quite well each other, exhibiting a good agreement with the simulation data in their respective domains of applicability, which are wider than what one might have anticipated. To put the work on a broader perspective, we have also carried out comparisons with numerical solutions of two integral equation theories, namely the PY and HNC theories. Both of them fail at low temperatures, but the HNC theory becomes very accurate and preferable to the PY theory at mod-

erate and large temperatures. The paper ends in Sec. VI with a discussion of the results and a perspective on the extension of the LT and HT approaches to the 3D case.

II. EXACT PROPERTIES

We consider in this paper a fluid of particles on a line interacting via the pairwise potential (1.1). Henceforth we take $\sigma = 1$ as the length unit and define the reduced temperature as $T^* \equiv k_B T / \epsilon$. Even in this one-dimensional case, the exact solution of the problem for arbitrary density and temperature is not known, the main difficulty lying in the fact that one particle can interact simultaneously with an arbitrary number of particles. Thus, it seems convenient to gain some insight by deriving a few exact results in limiting situations.

A. Low-density limit

Let us introduce the cavity function

$$y(r) = e^{\varphi(r)/k_B T} g(r), \quad (2.1)$$

where $g(r)$ is the radial distribution function. In general, $g(r)$ and $y(r)$ depend parametrically on density (ρ) and temperature (T^*). The virial expansion of the cavity function reads

$$y(r) = 1 + \sum_{n=1}^{\infty} y_n(r) \rho^n, \quad (2.2)$$

where the coefficients $y_n(r)$ depend parametrically on T^* and are represented by diagrams.^{26,27} In particular,

$$y_1(r) = \text{diagram of two open circles connected by a line}, \quad (2.3)$$

$$y_2(r) = \text{diagram of two open circles connected by a line with a filled circle in the middle} + 2 \times \text{diagram of two open circles connected by a line with a filled circle at one end} + \frac{1}{2} \times \text{diagram of two open circles connected by a line with a filled circle at both ends} + \frac{1}{2} \times \text{diagram of two open circles connected by a line with a filled circle at both ends and a diagonal line}. \quad (2.4)$$

Here, the open circles represent *root* points separated by a distance r , the filled circles represent *field* points to be integrated out, and each bond represents a Mayer function

$$f(r) = e^{-\varphi(r)/k_B T} - 1. \quad (2.5)$$

Thus, for instance,

$$\text{diagram of three open circles in a triangle} = \int dr_3 f(r_{13}) f(r_{23}), \quad (2.6)$$

$$\begin{array}{c} 3 \\ \diagup \quad \diagdown \\ 1 \quad 2 \end{array} 4 = \int d\mathbf{r}_3 \int d\mathbf{r}_4 f(r_{13})f(r_{34})f(r_{24})f(r_{14}). \quad (2.7)$$

So far, Eqs. (2.1)–(2.7) hold for any interaction potential and any dimensionality. In the special case of penetrable spheres, Eq. (2.1) yields

$$g(r) = \begin{cases} (1-x)y(r), & r < 1, \\ y(r), & r > 1, \end{cases} \quad (2.8)$$

where we have called

$$x \equiv 1 - e^{-1/T^*}. \quad (2.9)$$

Moreover, the Mayer function becomes

$$f(r) = xf_{\text{HS}}(r), \quad (2.10)$$

where

$$f_{\text{HS}}(r) = \begin{cases} -1, & r < 1, \\ 0, & r > 1, \end{cases} \quad (2.11)$$

is the Mayer function of hard spheres. Therefore, the spatial dependence of each one of the diagrams contributing to the virial expansion (2.2) is exactly the same as for hard spheres. The only difference is that each diagram is now multiplied by the temperature-dependent parameter x raised to a power equal to the number of bonds in that particular diagram.

In the special case of one-dimensional penetrable spheres (i.e., penetrable rods), it is not difficult to evaluate the integrals represented by the diagrams in Eqs. (2.3) and (2.4). The results are displayed in Table I. Note that diagram 2C is the square of diagram 1. All the functions are continuous everywhere and vanish for $r \geq 3$. At $r = 1$, diagrams 2A, 2B, and 2D have a second-order discontinuity. At $r = 2$, diagrams 1 and 2B have a first-order discontinuity, while 2C and 2D have a second-order discontinuity. Finally, 2A has a second-order discontinuity at $r = 3$.

Inserting the expressions displayed in Table I into Eqs. (2.3) and (2.4) we get the exact results shown in Table II. The discontinuities at $r = 1, 2$, and 3 are

$$y''(1^+) - y''(1^-) = -\rho^2 x^3 (3 - 4x + x^2) + \mathcal{O}(\rho^3), \quad (2.12)$$

$$y'(2^+) - y'(2^-) = \rho x^2 + \mathcal{O}(\rho^2), \quad (2.13)$$

$$y''(3^+) - y''(3^-) = \rho^2 x^3 + \mathcal{O}(\rho^3). \quad (2.14)$$

It is interesting to compare the exact density expansion with the HNC and PY approximations.^{26,27} In the HNC

Label	Diagram	$0 \leq r \leq 1$	$1 \leq r \leq 2$	$2 \leq r \leq 3$
1		$x^2(2-r)$	$x^2(2-r)$	0
2A		$-x^3(3-r^2)$	$-\frac{x^3}{2}(3-r)^2$	$-\frac{x^3}{2}(3-r)^2$
2B		$\frac{x^4}{2}(6-2r-r^2)$	$\frac{x^4}{2}(2-r)(4-r)$	0
2C		$x^4(2-r)^2$	$x^4(2-r)^2$	0
2D		$-x^5(3-2r)$	$-x^5(2-r)^2$	0

TABLE I: Explicit expressions of the diagrams contributing to $y_1(r)$ and $y_2(r)$.

approximation, the so-called bridge (or elementary) diagrams are neglected. To second order in density, the only bridge diagram in Table I is 2D. Therefore, the function $y_1(r)$ is retained but the function $y_2(r)$ is approximated by the function $y_2^{\text{HNC}}(r)$ given in Table II. In the PY approximation, apart from the bridge diagrams, a subset of the remaining diagrams is also neglected. In particular, the PY expression for $y_2(r)$ neglects diagrams 2C and 2D of Table I, what results in the function $y_2^{\text{PY}}(r)$ shown in Table II.

In the hard-rod limit ($\epsilon \rightarrow \infty$ or, equivalently, $T^* \rightarrow 0$ or $x \rightarrow 1$), the exact, HNC, and PY functions $y_2(r)$ reduce to the expressions also included in Table II. While the PY approximation for hard rods yields the exact pair correlation function for $r \geq 1$ (and this happens to any order in density because of a mutual cancelation of the neglected diagrams), we see that the PY cavity function fails inside the overlapping region ($r < 1$). In principle, this is not a serious drawback for strict hard rods, since $g(r) = 0$ for $r < 1$, regardless of the expression of the cavity function. However, if we consider penetrable rods at low temperature ($T^* \ll 1$ or $1-x \ll 1$), then $g(r)$ for $r < 1$ takes on relevant (although small) non-zero values, so that the expression of $\lim_{T^* \rightarrow 0} y_2^{\text{PY}}(r)$ for $r \leq 1$ anticipates the sort of limitations one can expect from the solution of the PY theory to penetrable-sphere models.^{13,14} It is worth noting that the second-order discontinuities at $r = 1$ of diagrams 2A, 2B, and 2D of Table I exactly compensate each other when those diagrams are added to get $\lim_{T^* \rightarrow 0} y_2(r)$. On the other hand, since diagram 2D is neglected in the HNC and PY approximations, an artificial second-order discontinuity at $r = 1$ remains in

Function	$0 \leq r \leq 1$	$1 \leq r \leq 2$	$2 \leq r \leq 3$
$y_1(r)$	$x^2(2-r)$	$x^2(2-r)$	0
$y_2(r)$	$-x^3(3-r^2) + x^4(8-4r-\frac{1}{2}r^2) - x^5(\frac{3}{2}-r)$	$-\frac{x^3}{2}(r-3)^2 + x^4(2-r)(5-\frac{3}{2}r) - \frac{x^5}{2}(r-2)^2$	$-\frac{x^3}{2}(r-3)^2$
$y_2^{\text{HNC}}(r)$	$-x^3(3-r^2) + x^4(8-4r-\frac{1}{2}r^2)$	$-\frac{x^3}{2}(r-3)^2 + x^4(2-r)(5-\frac{3}{2}r)$	$-\frac{x^3}{2}(r-3)^2$
$y_2^{\text{PY}}(r)$	$-x^3(3-r^2) + x^4(6-2r-r^2)$	$-\frac{x^3}{2}(r-3)^2 + x^4(2-r)(4-r)$	$-\frac{x^3}{2}(r-3)^2$
$\lim_{T^* \rightarrow 0} y_2(r)$	$\frac{1}{2}r^2 - 3r + \frac{7}{2}$	$\frac{1}{2}r^2 - 3r + \frac{7}{2}$	$-\frac{1}{2}(r-3)^2$
$\lim_{T^* \rightarrow 0} y_2^{\text{HNC}}(r)$	$\frac{1}{2}r^2 - 4r + 5$	$r^2 - 5r + \frac{11}{2}$	$-\frac{1}{2}(r-3)^2$
$\lim_{T^* \rightarrow 0} y_2^{\text{PY}}(r)$	$3 - 2r$	$\frac{1}{2}r^2 - 3r + \frac{7}{2}$	$-\frac{1}{2}(r-3)^2$

TABLE II: Explicit expressions of the functions $y_1(r)$ and $y_2(r)$. The first, second, and fifth rows are exact results, while the third, fourth, sixth, and seventh rows correspond to the HNC and PY approximations.

those approximations. It is interesting to point out that, although the hard-rod interaction ($\epsilon \rightarrow \infty$) is more singular than the penetrable-rod interaction ($\epsilon = \text{finite}$), the cavity function $y(r)$ of the former is paradoxically analytic at $r = 1$, while that of the latter presents a second-order discontinuity. When considering the radial distribution function $g(r)$, however, a jump discontinuity exists in both cases.

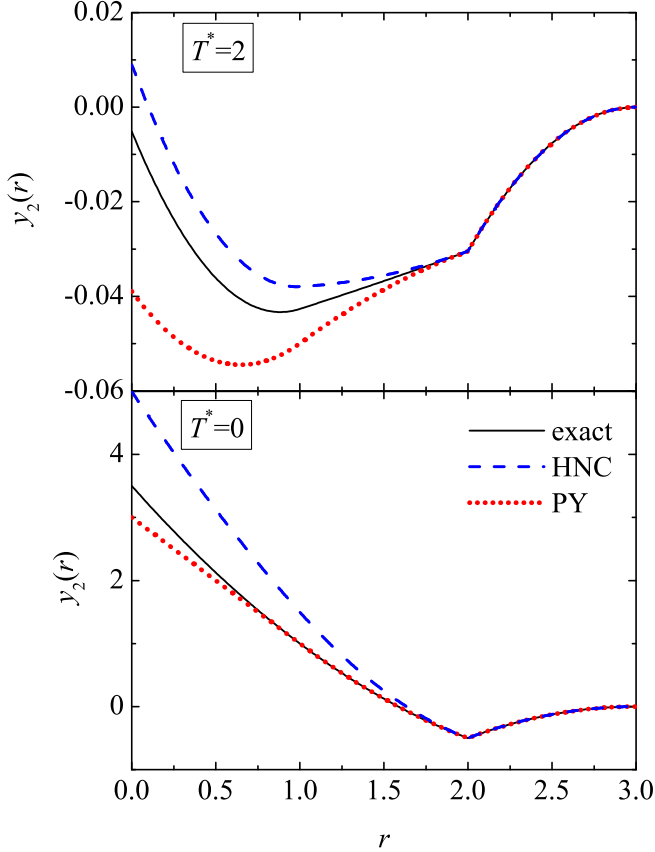


FIG. 1: (Color online) Plot of the virial coefficient $y_2(r)$ at $T^* = 2$ (top panel) and $T^* = 0$ (bottom panel). The solid lines are the exact results, the dashed lines are the HNC predictions, and the dotted lines are the PY predictions.

Figure 1 compares the exact function $y_2(r)$ with the HNC and PY approximations at $T^* = 2$ and $T^* = 0$. Although restricted to low densities and one-dimensional

systems, Fig. 1 clearly illustrates some of the general features found in three-dimensional penetrable spheres at finite densities:^{13,14} the PY underestimates the penetrability effect ($r < 1$), while the HNC approximation overestimates it. Moreover, the HNC theory tends to be better at higher temperatures, while the PY is preferable at lower temperatures. If we characterize the quality of each approximation by the separation of the corresponding $y_2(0)$ from the exact result, it turns out that the temperature beyond which the HNC approximation becomes better than the PY approximation is $T^* = 1/\ln 3 \simeq 0.91$. If we take instead $y_2(1)$ as the characteristic quantity, then the preceding temperature is replaced by $T^* = 1/\ln 2 \simeq 1.44$. In either case, $T^* \approx 1$ seems to be the typical temperature beyond which the HNC approximation prevails over the PY one. This will be confirmed later in Sec. V.

Although in this paper we are more interested in the structural properties than in the thermodynamic ones, it is worthwhile obtaining the first four virial coefficients as functions of temperature. For penetrable rods, the compressibility factor Z , the isothermal susceptibility χ , and the excess internal energy per particle u_{ex} are related to the cavity function as follows:

$$Z \equiv \frac{\beta p}{\rho} = 1 + \rho x y(1), \quad (2.15)$$

$$\chi \equiv \left(\beta \frac{\partial p}{\partial \rho} \right)^{-1} = 1 + 2\rho \left\{ \int_0^1 dr [(1-x)y(r) - 1] + \int_1^\infty dr [y(r) - 1] \right\}, \quad (2.16)$$

$$u_{\text{ex}} = \rho \epsilon (1-x) \int_0^1 dr y(r), \quad (2.17)$$

where p is the pressure and $\beta \equiv 1/k_B T$. The virial coefficients $B_n(x)$ are defined by the density expansion

$$Z = 1 + \sum_{n=2}^{\infty} B_n(x) \rho^{n-1}. \quad (2.18)$$

Inserting the exact cavity function to second order in density into Eqs. (2.15)–(2.17), and taking into account the thermodynamic relations $\chi^{-1} = \partial(\rho Z)/\partial \rho$ and

Theory	$B_4(x)$	$B_4(1)$	T_0^*	T_{\min}^*	$B_4 _{\min}$
Exact	$-x^4(2 - \frac{7}{2}x + \frac{1}{2}x^2)$	1	1.0120	1.4427	-0.02344
PY-v	$-x^4(2 - 3x)$	1	0.9102	1.3121	-0.03236
PY-c	$-x^4(\frac{4}{3} - \frac{7}{3}x)$	1	1.1802	1.6369	-0.01165
PY-e	$-x^4(2 - \frac{14}{5}x)$	$\frac{4}{5}$	0.7982	1.1802	-0.04265
HNC-v, HNC-e	$-x^4(2 - \frac{7}{2}x)$	$\frac{3}{2}$	1.1802	1.6369	-0.01747
HNC-c	$-x^4(2 - \frac{35}{12}x)$	$\frac{11}{12}$	0.8640	1.2573	-0.03622

TABLE III: Fourth virial coefficient $B_4(x)$ and other related quantities as given exactly and by the PY and HNC approximations through the virial (v), compressibility (c), and energy (e) routes.

$\rho \partial u_{\text{ex}} / \partial \rho = \partial Z / \partial \beta$, one consistently gets $B_2(x) = x$, $B_3(x) = x^3$, and the fourth virial coefficient $B_4(x)$ displayed in Table III. On the other hand, insertion of $y^{\text{PY}}(r)$ yields a different $B_4(x)$ depending on whether the virial (v) route (2.15), the compressibility (c) route (2.16), or the energy (e) route (2.17) is used. This internal inconsistency is also present in the case of $y^{\text{HNC}}(r)$, except that now the virial and energy routes are equivalent.²⁸ These approximate expressions for the fourth virial coefficient are also included in Table III. The exact and the approximate $B_4(x)$ share the properties of changing sign at a certain temperature T_0^* and having a (negative) minimum value $B_4|_{\min}$ at a higher temperature T_{\min}^* . Only the PY-v and PY-c approximations are consistent with the exact hard-rod value $B_4(1) = 1$, while only the PY-c approximation fails to yield the correct limit $B_4 \rightarrow -2x^4$ for high temperatures. From Table III one can conclude that the best global agreement with the exact $B_4(x)$ is achieved by the PY-v approximation. It is interesting to note that, while the energy route to the equation of state is ill defined for hard spheres, one can circumvent this problem by first getting $B_4(x)$ through the energy route and then taking the zero-temperature limit $\lim_{x \rightarrow 1} B_4(x)$. The fact that $B_4^{\text{PY-e}}(1) \neq B_4^{\text{PY-v}}(1)$ shows that the equivalence between the energy and virial routes proven in Ref. 29 when hard spheres are obtained from the square-shoulder potential does not hold when hard spheres are obtained from penetrable spheres.

B. High-temperature limit

In the high-temperature limit ($T^* \rightarrow \infty$), the parameter defined by Eq. (2.9) tends to zero, i.e., $x \approx 1/T^* \rightarrow 0$. Since a diagram having m bonds is of order x^m , we can neglect all the diagrams contributing to a given coefficient $y_n(r)$, except the one having the least number of bonds (namely, $m = n + 1$ bonds). In other words, only the linear chain diagrams survive.¹⁸

$$\begin{aligned}
y_n(r_{12}) &\rightarrow \text{O} \text{---} \text{3} \text{---} \text{4} \text{---} \dots \text{---} \text{n+2} \text{---} \text{O} \\
&= x^{n+1} \int d\mathbf{r}_3 \int d\mathbf{r}_4 \dots \int d\mathbf{r}_{n+2} \\
&\quad \times f_{\text{HS}}(r_{13}) f_{\text{HS}}(r_{34}) \dots f_{\text{HS}}(r_{n+2,2}) \quad (2.19)
\end{aligned}$$

In Fourier space,

$$\tilde{y}_n(k) \rightarrow x^{n+1} [\tilde{f}_{\text{HS}}(k)]^{n+1}, \quad (2.20)$$

where $\tilde{f}_{\text{HS}}(k)$ is the Fourier transform of the hard-sphere Mayer function (2.11). From Eqs. (2.2) and (2.20) it is straightforward to get the Fourier transform of $y(r) - 1$, so that we finally have

$$y(r) \rightarrow 1 + xw(r), \quad (2.21)$$

where $w(r)$ is the inverse Fourier transform of

$$\tilde{w}(k) = \rho x \frac{[\tilde{f}_{\text{HS}}(k)]^2}{1 - \rho x \tilde{f}_{\text{HS}}(k)}. \quad (2.22)$$

The limit result (2.21) can be written in a number of equivalent ways. For instance, the total correlation function $h(r) \equiv g(r) - 1$ becomes, on account of Eqs. (2.8), (2.11), and (2.21),

$$h(r) \rightarrow x[w(r) + f_{\text{HS}}(r)]. \quad (2.23)$$

In Fourier space,

$$\tilde{h}(k) \rightarrow x \frac{\tilde{f}_{\text{HS}}(k)}{1 - \rho x \tilde{f}_{\text{HS}}(k)}, \quad (2.24)$$

where use has been made of Eq. (2.22). From Eq. (2.24) it is straightforward to get the structure factor $S(k) = 1 + \rho \tilde{h}(k)$, as well as the Fourier transform $\tilde{c}(k) = \tilde{h}(k)/S(k)$:

$$S(k) \rightarrow \frac{1}{1 - \rho x \tilde{f}_{\text{HS}}(k)}, \quad \tilde{c}(k) \rightarrow x \tilde{f}_{\text{HS}}(k). \quad (2.25)$$

The last expression in Eq. (2.25) is equivalent to $c(r) \rightarrow f(r)$.

The asymptotic behaviors (2.21)–(2.25) are of mean-field type^{7,30,31,32,33} and hold in the combined limit $T^* \rightarrow \infty$, $\rho \rightarrow \infty$ with $\rho x \approx \rho/T^* = \text{fixed}$ for any dimensionality. In the one-dimensional case, one simply has

$$\tilde{f}_{\text{HS}}(k) = -2 \sin k/k, \quad (2.26)$$

so that

$$w(r) = \frac{1}{\pi} \int_0^\infty dk \cos kr \tilde{w}(k), \quad \tilde{w}(k) = \frac{4\rho x \sin^2 k}{k^2 + 2\rho x k \sin k}. \quad (2.27)$$

It is proven in the Appendix that the density expansion of $w(r)$ is

$$w(r) = \sum_{n=2}^\infty (\rho x)^{n-1} w_n(r), \quad (2.28)$$

where

$$w_n(r) = n \sum_{m=0}^n \frac{(-1)^{n+m}}{m!(n-m)!} (n-2m-r)^{n-1} \Theta(n-2m-r), \quad (2.29)$$

$\Theta(x)$ being the Heaviside step function. It is also shown that

$$2 \frac{w_n(1)}{n} = -\frac{w_{n+1}(0)}{n+1}, \quad n \geq 2, \quad (2.30)$$

this property being needed to prove the thermodynamic consistency between the virial and energy routes to the equation of state.¹⁸

The virial series (2.28) converges for $\rho x < \nu(r)$, where $1/\nu(r) = \lim_{n \rightarrow \infty} |w_{n+1}(r)/w_n(r)|$. Equation (2.30) implies that $\nu(0) = \nu(1)$, but otherwise the radius of convergence $\nu(r)$ could in principle be r -dependent. We have numerically checked that this is not the case and that $\nu(r) = \frac{1}{2}$ regardless of the value of r . From Eq. (2.27) we see that the radius of convergence $\nu(r) = \frac{1}{2}$ is a consequence of the mathematical singularity of $w(r)$ at the negative density $2\rho x = -1$. Therefore, we conclude that in the high-temperature domain the virial expansion of the cavity function converges uniformly for $\rho < 1/2x \approx T^*/2$.

Using Eqs. (2.21) and (2.28) in Eq. (2.15), we obtain the virial expansion of the equation of state in the high-temperature limit,

$$\frac{p}{\rho k_B T} \rightarrow 1 + \rho x + \sum_{n=3}^\infty \rho^{n-1} x^n w_{n-1}(1), \quad (2.31)$$

so that the virial coefficients are $B_2(x) = x$ and $B_n(x) \rightarrow x^n w_{n-1}(1)$ for $n \geq 3$. Therefore, the virial series of the equation of state converges for $\rho < (2x)^{-1}$ in the high-temperature limit.

By an adequate reordering of terms (see the Appendix), the function $w(r)$ can be written in real space as

$$w(r) = \Theta(1-r) + 2 \sum_{p=1}^\infty (-1)^p J'_p(2\rho x(p-r)) \Theta(p-r), \quad (2.32)$$

where $J'_p(z)$ is the first derivative of the Bessel function of the first kind $J_p(z)$.³⁴ In particular, in the overlapping region ($r < 1$), we have

$$w(r < 1) = 1 + 2 \sum_{p=1}^\infty (-1)^p J'_p(2\rho x(p-r)). \quad (2.33)$$

Likewise, in the shell $n < r < n+1$ with $n \geq 1$,

$$w(n < r < n+1) = 2 \sum_{p=n+1}^\infty (-1)^p J'_p(2\rho x(p-r)). \quad (2.34)$$

Using known properties of the Bessel functions it is possible to derive some exact results. For instance, the second-order, first-order, and second-order discontinuities of $w(r)$ at $r = 1, 2$, and 3 , respectively, are

$$w''(1^+) - w''(1^-) = -3(\rho x)^2, \quad (2.35)$$

$$w'(2^+) - w'(2^-) = \rho x, \quad (2.36)$$

$$w''(3^+) - w''(3^-) = (\rho x)^2. \quad (2.37)$$

Equations (2.35)–(2.37) give the singularities of the cavity function for any density in the high-temperature limit. Of course, they are compatible with Eqs. (2.12)–(2.14) for low densities. Other interesting results are

$$w'(1) = \rho x [w(0) - w(2) - 1], \quad (2.38)$$

$$w'(2^+) = \rho x [w(1) - w(3)], \quad (2.39)$$

$$w'(n) = \rho x [w(n-1) - w(n+1)], \quad n \geq 3. \quad (2.40)$$

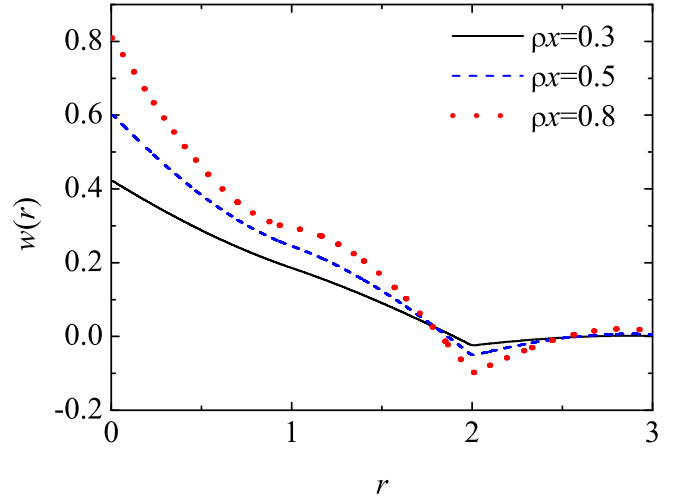


FIG. 2: (Color online) Plot of the function $w(r)$ at $\rho x = 0.3$, 0.5 , and 0.8 .

Although the series representation (2.32) is useful to derive explicit results and seems to converge for any value of ρx , it is more practical to use the integral representation (2.27) from a computational point of view. Figure 2 shows the function $w(r)$ for $\rho x = 0.3$, $\rho x = 0.5$, and $\rho x = 0.8$. As expected, the function $w(r)$ becomes more structured as the product ρx grows.

C. Zero-temperature limit: Hard rods

The correlation functions for one-dimensional fluids with interactions restricted to nearest neighbors are exactly known.^{25,35,36,37,38,39} However, as indicated in Sec. I, the bounded nature of the potential (1.1) allows for multiple pair interactions and, as a consequence, the interactions are obviously not restricted to nearest neighbors.

On the other hand, as the temperature is lowered, the occurrence of simultaneous overlapping of three or more particles becomes less and less likely and the nearest-neighbor approximation becomes more and more accurate, until the exact result is obtained at zero temperature (hard-rod limit). In that limit ($T^* = 0$ or $x = 1$), the radial distribution function $g(r)$ vanishes inside the core ($r < 1$) but the cavity function $y(r)$ does not and so special care must be taken to get $\lim_{T^* \rightarrow 0} y(r)$ as a function of density for $r < 1$. As already recognized by Stell,⁴⁰ in order to get the hard-sphere cavity function for $r < 1$ one must take the limit of a suitably parameterized non-singular potential.

We start by recalling the exact solution in the case of nearest-neighbor interactions. At arbitrary density and temperature, the one-dimensional radial distribution function can be written as^{38,39}

$$g(r) = \frac{1}{\rho} \sum_{n=1}^{\infty} p_n(r), \quad (2.41)$$

where $p_n(r)$ is the probability density distribution that the n -th neighbor of a given particle is a distance r apart. The distributions $\{p_n(r)\}$ obey the recursive relation

$$p_n(r) = \int_0^r dr' p_{n-1}(r') p_1(r - r'), \quad n \geq 2. \quad (2.42)$$

The explicit form of the nearest-neighbor probability distribution is

$$p_1(r) = K e^{-\varphi(r)/k_B T} e^{-\xi r}, \quad (2.43)$$

where the amplitude K and the damping constant ξ will be determined later on.

The convolution in (2.42) suggests the introduction of the Laplace transforms

$$P_n(t) = \int_0^{\infty} dr e^{-rt} p_n(r), \quad G(t) = \int_0^{\infty} dr e^{-rt} g(r). \quad (2.44)$$

Thus, Eq. (2.42) yields

$$P_n(t) = P_{n-1}(t) P_1(t) = P_1^n(t), \quad n \geq 2. \quad (2.45)$$

When this is introduced into Eq. (2.41) one gets

$$G(t) = \frac{1}{\rho} \sum_{n=1}^{\infty} [P_1(t)]^n = \frac{1}{\rho} \frac{P_1(t)}{1 - P_1(t)}. \quad (2.46)$$

From Eq. (2.43), it is obtained

$$P_1(t) = K \Omega(t + \xi), \quad (2.47)$$

where

$$\Omega(t) = \int_0^{\infty} dr e^{-rt} e^{-\varphi(r)/k_B T} \quad (2.48)$$

is the Laplace transform of $\exp[-\varphi(r)/k_B T]$.

To close the solution, one needs to determine the parameters K and ξ . This is done by imposing basic consistency conditions. The relationship between $G(t)$ and the Laplace transform $H(t)$ of the total correlation function $h(r) = g(r) - 1$ is

$$G(t) = \frac{1}{t} + H(t). \quad (2.49)$$

Since $H(t)$ must be finite at $t = 0$ (from the compressibility route to the equation of state), it follows that

$$G(t) = \frac{1}{t} + \mathcal{O}(t^0), \quad P_1(t) = 1 - \frac{1}{\rho} t + \mathcal{O}(t^2). \quad (2.50)$$

The last equality in (2.50) implies that $P_1(0) = 1$ and $P_1'(0) = -1/\rho$. Hence, $K = 1/\Omega(\xi)$ and ξ is the solution of the equation

$$\frac{\Omega'(\xi)}{\Omega(\xi)} = -\frac{1}{\rho}. \quad (2.51)$$

We emphasize that Eqs. (2.41)–(2.51) provide the exact solution only in the case of nearest-neighbor interactions. Let us now “forget” for the moment that the penetrable-sphere potential (1.1) is not restricted to nearest neighbors and apply the above scheme to it. In that approximation, Eqs. (2.43) and (2.48) yield

$$p_1(r) = K e^{-\xi r} [1 - x + x \Theta(r - 1)], \quad (2.52)$$

$$\Omega(t) = \frac{1 - x + x e^{-t}}{t}. \quad (2.53)$$

The damping coefficient ξ is the solution of the transcendental equation (2.51), i.e.,

$$\frac{x}{1 - x} (\xi - \xi') e^{-\xi} = \xi', \quad (2.54)$$

where we have called

$$\xi' \equiv \frac{\xi}{\rho} - 1. \quad (2.55)$$

In addition, the amplitude K becomes

$$K = \frac{\xi' e^{\xi}}{x} \quad (2.56)$$

and Eq. (2.47) gives

$$P_1(t) = \frac{\xi - \xi' + \xi' e^{-t}}{t + \xi}. \quad (2.57)$$

Inserting this into (2.46) and expanding in powers of e^{-t} , we get

$$\rho G(t) = \frac{\xi - \xi'}{t + \xi'} + \sum_{n=1}^{\infty} \xi'^n \left[\frac{1}{(t + \xi')^n} + \frac{\xi - \xi'}{(t + \xi')^{n+1}} \right] e^{-nt}. \quad (2.58)$$

Its Laplace inversion yields

$$g(r) = \sum_{n=0}^{\infty} \psi_n(r-n) \Theta(r-n), \quad (2.59)$$

where

$$\psi_n(r) = \frac{\xi'^n}{\rho} \frac{e^{-\xi' r} r^{n-1}}{n!} [n + (\xi - \xi')r]. \quad (2.60)$$

In particular, using Eq. (2.8), the cavity function inside the core is, in this nearest-neighbor approximation,

$$y(r < 1) = \frac{\psi_0(r)}{1-x} = \frac{\xi - \xi'}{\rho(1-x)} e^{-\xi' r}. \quad (2.61)$$

Of course, Eqs. (2.52)–(2.61) are not exact at finite temperature. However, they become exact in the hard-rod limit ($T^* \rightarrow 0$ or $x \rightarrow 1$). In that limit, the solution of Eq. (2.54) is $\xi = \xi_0 - \xi_0^2 e^{\xi_0} (1-x) + \dots$, so that $\xi' = \xi - \xi_0 e^{\xi_0} (1-x) + \dots$, where

$$\xi_0 \equiv \frac{\rho}{1-\rho}. \quad (2.62)$$

Therefore,

$$\lim_{T^* \rightarrow 0} \psi_n(r) = \frac{\xi_0^n}{\rho(n-1)!} e^{-\xi_0 r} r^{n-1}, \quad n \geq 1, \quad (2.63)$$

$$\lim_{T^* \rightarrow 0} y(r < 1) = \frac{\xi_0}{\rho} e^{-\xi_0(r-1)}. \quad (2.64)$$

The final explicit expression of the cavity function for hard rods is then

$$\begin{aligned} \lim_{T^* \rightarrow 0} y(r) &= \frac{\xi_0}{\rho} e^{-\xi_0(r-1)} + \sum_{n=2}^{\infty} \frac{\xi_0^n}{\rho(n-1)!} e^{-\xi_0(r-n)} \\ &\quad \times (r-n)^{n-1} \Theta(r-n). \end{aligned} \quad (2.65)$$

This equation not only gives the exact hard-rod radial distribution function $g(r) = y(r)\Theta(r-1)$, but also the cavity function inside the hard core ($r < 1$). Interestingly enough, $y(r)$ for $r < 1$ is just the analytical continuation of its expression for $1 < r < 2$, so that $y(r)$ is analytical at $r = 1$, even though the potential is highly singular at that point. This singularity manifests itself at $r = n$ with $n \geq 2$, where $y(r) = g(r)$ presents a discontinuity of order $n-1$.

We are not aware of any previous derivation of Eq. (2.64). By expanding in powers of density, it is easy

to verify that Eq. (2.65) is consistent with the exact $\lim_{T^* \rightarrow 0} y_1(r)$ and $\lim_{T^* \rightarrow 0} y_2(r)$ given in Table II. As a further test of the exact character of Eq. (2.64), let us check the fulfillment of the following two zero-separation theorems,⁴¹ as applied to hard rods,

$$\ln y(0) = \frac{1}{k_B T} \mu_{\text{ex}}, \quad (2.66)$$

$$\left. \frac{\partial \ln y(r)}{\partial r} \right|_{r=0} = -\rho y(1). \quad (2.67)$$

In Eq. (2.66), μ_{ex} is the excess chemical potential, which is given by

$$\frac{1}{k_B T} \mu_{\text{ex}} = Z(\rho) - 1 + \int_0^\rho d\rho' \frac{Z(\rho') - 1}{\rho'}, \quad (2.68)$$

where $Z = 1 + \rho y(1)$ is the hard-rod compressibility factor [cf. Eq. (2.15)]. Since $y(1) = 1/(1-\rho)$, Eqs. (2.66) and (2.67) imply that

$$y(0) = \frac{e^{\rho/(1-\rho)}}{1-\rho} = y(1) e^{\rho y(1)}, \quad (2.69)$$

$$\left. \frac{\partial \ln y(r)}{\partial r} \right|_{r=0} = -\frac{\rho}{1-\rho}. \quad (2.70)$$

It is straightforward to check that Eq. (2.64) verifies both (2.69) and (2.70).

In a general one-dimensional system, the Fourier transforms of the total and direct correlation functions can be obtained from the Laplace transform of the radial distribution function as

$$\tilde{h}(k) = G(t = ik) + G(t = -ik), \quad \tilde{c}(k) = \frac{\tilde{h}(k)}{1 + \rho \tilde{h}(k)}. \quad (2.71)$$

Inserting Eq. (2.57) into Eq. (2.46) and taking the zero-temperature limit one finally gets

$$\lim_{T^* \rightarrow 0} \tilde{c}(k) = -\frac{2\xi_0}{\rho} \left[\xi_0 \frac{1 - \cos k}{k^2} + \frac{\sin k}{k} \right], \quad (2.72)$$

$$\lim_{T^* \rightarrow 0} c(r) = -\frac{1-\rho r}{(1-\rho)^2} \Theta(1-r). \quad (2.73)$$

The bridge function is defined as²⁷ $B(r) = \ln y(r) + c(r) - h(r)$. Therefore, Eqs. (2.64) and (2.73) yield

$$\lim_{T^* \rightarrow 0} B(r < 1) = -\frac{\rho(1-\rho r)}{(1-\rho)^2} - \ln(1-\rho). \quad (2.74)$$

As is well known, the PY theory yields the exact correlation functions $g(r)$ and $c(r)$ for hard rods.^{24,25,40} However, it provides a wrong cavity function $y(r)$ inside the hard core, as already seen to order ρ^2 in Sec. II A. To

show this for finite densities, we recall that the PY approximation consists of the closure²⁷ $y(r) = g(r) - c(r)$. Therefore,

$$\lim_{T^* \rightarrow 0} y^{\text{PY}}(r < 1) = -c(r < 1) = \frac{1 - \rho r}{(1 - \rho)^2}. \quad (2.75)$$

This result, which gives rise to a second-order discontinuity at $r = 1$, differs markedly from the exact result (2.64). The PY cavity function $\lim_{T^* \rightarrow 0} y^{\text{PY}}(r)$ verifies the zero-separation theorem (2.70) but not (2.69). As for the PY bridge function inside the core, the result is

$$\lim_{T^* \rightarrow 0} B^{\text{PY}}(r < 1) = -\frac{\rho(2 - r - \rho)}{(1 - \rho)^2} + \ln \frac{1 - \rho r}{(1 - \rho)^2}, \quad (2.76)$$

which differs from Eq. (2.74).

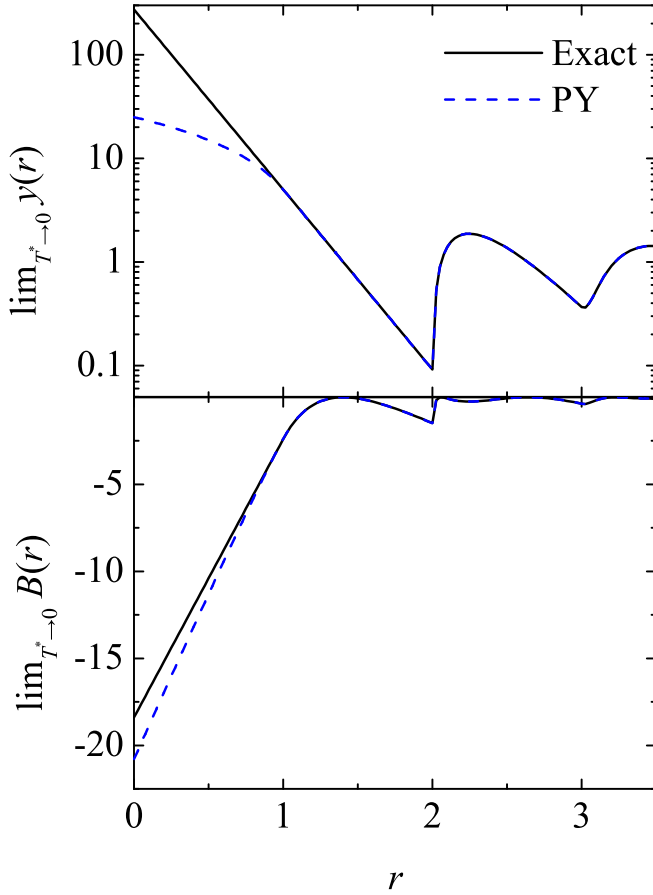


FIG. 3: (Color online) Plot of the cavity function $y(r)$ and the bridge function $B(r)$ in the hard-rod limit at $\rho = 0.8$. The solid lines are the exact results, while the dashed lines are the PY predictions.

Figure 3 shows $\lim_{T^* \rightarrow 0} y(r)$ and $\lim_{T^* \rightarrow 0} B(r)$ at $\rho = 0.8$. It clearly illustrates the tendency of the PY approximation to underestimate the cavity function inside the core, a feature that continues to hold in the case of three-dimensional penetrable spheres.¹³ It is also quite apparent that the HNC closure $B(r) = 0$ is far from being accurate in the hard-rod limit, especially for $r < 1$.

Before closing this Section it is worthwhile noting a flaw in the “proof” given in Ref. 25 on the exact character of Eq. (2.75). It is first proven that the PY closure is consistent with the exact hard-core radial distribution function or, equivalently, with the exact cavity function for $r > 1$. Next, taking the limit $r \rightarrow 1^+$ and taking into account the continuity of $y(r)$ at $r = 1$, it is argued that

$$\begin{aligned} \frac{1 - \rho r}{(1 - \rho)^2} &= \lim_{r \rightarrow 1^+} \lim_{T^* \rightarrow 0} y(r) = \lim_{r \rightarrow 1^-} \lim_{T^* \rightarrow 0} y(r) \\ &= \lim_{T^* \rightarrow 0} y(r < 1). \end{aligned} \quad (2.77)$$

While the two first equalities are entirely correct, the third one is not justified in general, so that the conclusion that $\lim_{T^* \rightarrow 0} y(r < 1) = \lim_{T^* \rightarrow 0} y^{\text{PY}}(r < 1)$ is flawed.

III. HIGH-TEMPERATURE APPROXIMATION

In the limit of asymptotically high temperatures, the cavity function becomes the mean-field result (2.21), where the function $w(r)$, which in the one-dimensional case is given by Eqs. (2.27) or (2.32), depends on density and temperature through the product ρx only. It is then natural to expect that the simple ansatz

$$y(r) = 1 + xw(r) \quad (3.1)$$

constitutes a good approximation for sufficiently large temperatures. As a matter of fact, comparison with three-dimensional simulation results shows that this indeed the case for $T^* > 3$.⁷

The approximation (3.1) neglects all the diagrams different from the linear chain ones. A better approximation can be expected by making

$$y(r) = \exp[xw(r)], \quad (3.2)$$

which reduces to (2.21) in the limit $x \rightarrow 0$. In addition to the linear chain diagrams, the approximation (3.2) retains all the reducible diagrams that factorize into linear chain diagrams. In particular, (3.2) implies that

$$y_2(r) = \text{[diagram 1]} + \frac{1}{2} \text{[diagram 2]}, \quad (3.3)$$

$$y_3(r) = \text{[diagram 1]} + \text{[diagram 2]} + \frac{1}{6} \text{[diagram 3]}. \quad (3.4)$$

A third possibility is the Padé approximant

$$y(r) = \frac{1}{1 - xw(r)}. \quad (3.5)$$

In that case, the diagrams retained are the same as in the approximation (3.2), except that the numerical factors in front of the reducible diagrams are larger. For instance, the factors affecting the second diagram of Eq. (3.3) and the second and third diagrams of Eq. (3.4) are 1 (instead of $\frac{1}{2}$), 2 (instead of 1), and 1 (instead of $\frac{1}{6}$), respectively. This can be interpreted as an effective way of compensating for the neglected diagrams.

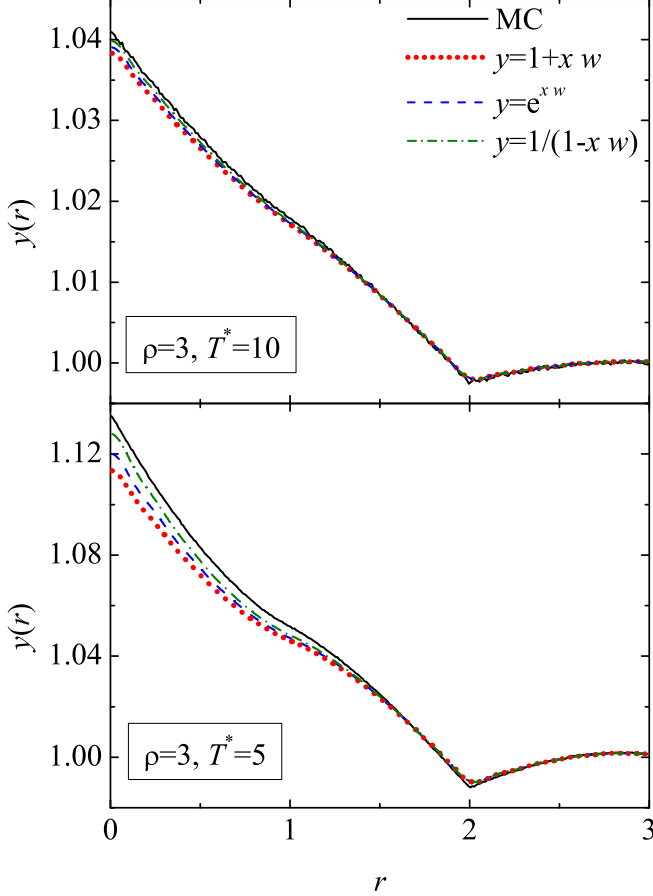


FIG. 4: (Color online) Plot of the cavity function $y(r)$ at $\rho = 3$ and $T^* = 10$ (top panel) and $T^* = 5$ (bottom panel). The solid lines are results obtained from MC simulations, the dotted lines represent the approximation (3.1), the dashed lines represent the approximation (3.2), and the dashed-dotted lines represent the approximation (3.5).

The three heuristic approximations (3.1), (3.2), and (3.5), among other possible ones, have the potential of describing satisfactorily well the structure of penetrable-rod fluids at sufficiently high temperatures. To test this expectation and also to determine which approximation is the most accurate one, we have compared them with MC simulations at $T^* = 10$ and $T^* = 5$ in Fig. 4. It can be observed that the three approximations tend to underestimate the correlation function for $r < 2$, this effect becoming more pronounced as the temperature decreases. On the other hand, the Padé approximant (3.5) is closer to the MC curves than the exponential approximation

(3.2) and the linear approximation (3.1). Therefore, in what remains we will adopt Eq. (3.5), supplemented by Eq. (2.27), as our high-temperature (HT) approximation. The highest value of $w(r)$ occurs at $r = 0$ and is an increasing function of ρx . For $\rho x \leq 1.1$ one has $w(0) \leq 1$ and so Eq. (3.5) is mathematically well defined for any temperature if $\rho x \leq 1.1$. This is the range where the fluid is expected to be stable against the solid.¹⁸

IV. LOW-TEMPERATURE APPROXIMATION

A. Construction of the approximation

We have already mentioned that the automatic translation to penetrable rods [cf. Eqs. (2.52)–(2.61)] of the scheme valid for nearest-neighbor interactions does not yield the exact correlation functions, except at zero temperature. On the other hand, one might reasonably wonder whether Eqs. (2.52)–(2.61) constitute a good approximation for (non-zero) low temperatures (i.e., $T^* \ll 1$ or $1 - x \ll 1$). A drawback of the approximation (2.52)–(2.61), however, is that it yields a cavity function that has a jump at $r = 1$, i.e., $y(1^+) \neq y(1^-)$, while the exact $y(r)$ and its first derivative must be continuous at $r = 1$.

The failure to satisfy the condition $y(1^+) = y(1^-)$ can be traced back to the constraint (2.54), which is a consequence of imposing the physical requirements (2.50) on the approximation (2.46)–(2.48) for non-nearest-neighbor interactions. Nevertheless, the form (2.57) satisfies Eq. (2.50) for arbitrary ξ , provided ξ' is still defined by Eq. (2.55). This strongly suggests to maintain Eq. (2.57), except that now the parameter ξ is not tied to satisfy Eq. (2.54) but is instead determined from the condition $y(1^+) = y(1^-)$. Since this is not enough to guarantee that $y'(1^+) = y'(1^-)$, we complement the above approximation by adding a linear function in the shell $0 < r < 1$. In summary, our *low-temperature* (LT) approximation consists of

$$g(r) = (r-1)A\Theta(1-r) + \sum_{n=0}^{\infty} \psi_n(r-n)\Theta(r-n), \quad (4.1)$$

where the functions $\psi_n(r)$ are given by Eq. (2.60), ξ' being defined by Eq. (2.55). The LT approximation (4.1) contains two free parameters (ξ and A) to be determined, as indicated before, from the continuity conditions of $y(r)$ at $r = 1$. To that end, note that

$$y(r < 1) = \frac{A}{1-x}(r-1) + \frac{\xi - \xi'}{\rho(1-x)}e^{-\xi'r}, \quad (4.2)$$

$$y(1 < r < 2) = \frac{\xi - \xi'}{\rho}e^{-\xi'r} + \frac{\xi'}{\rho}[1 + (\xi - \xi')(r-1)] \times e^{-\xi'(r-1)}. \quad (4.3)$$

Now, the condition $y(1^+) = y(1^-)$ yields the following transcendental equation for the parameter ξ :

$$\frac{x}{1-x}(\xi - \xi')e^{-\xi'} = \xi', \quad (4.4)$$

which differs from Eq. (2.54) in the replacement of $e^{-\xi}$ by $e^{-\xi'}$. Finally, the condition $y'(1^+) = y'(1^-)$ determines the parameter A as

$$A = \frac{1-x}{\rho} \xi'(\xi - \xi'). \quad (4.5)$$

This closes the construction of the LT approximation. It is given by Eq. (4.1), supplemented by Eqs. (2.55), (2.60), (4.4), and (4.5).

The Laplace transform of Eq. (4.1) is

$$G(t) = A \frac{1-t-e^{-t}}{t^2} + \frac{1}{\rho} \frac{P_1(t)}{1-P_1(t)}, \quad (4.6)$$

where the function $P_1(t)$ is given by Eq. (2.57) but now it cannot be interpreted simply as the Laplace transform of the nearest-neighbor probability distribution. As already mentioned, the LT approximation (4.6) fulfills the physical condition (2.50).

r	$y(r)$	$y'(r)$
0	$\xi' e^{\xi'} [1 - (1-x)\xi'] / \rho x$	$-\xi'^2 e^{\xi'} / \rho$
1	$\xi' / \rho x$	$-\xi'^2 [1 - (1-x)e^{\xi'}] / \rho x$
2 ⁻	$\xi' [(1-x)\xi' + e^{-\xi'}] / \rho x$	$-\xi'^2 [e^{-\xi'} - (1-x)(1-\xi')] / \rho x$
2 ⁺	$\xi' [(1-x)\xi' + e^{-\xi'}] / \rho x$	$\xi'^2 [1 - (1-x)\xi' - e^{-\xi'}] / \rho x$

TABLE IV: Values of the cavity function and its first derivative at $r = 0, 1$, and 2 in the LT approximation (4.1).

As an application of the explicit character of the LT approximation (4.1), we give in Table IV the values of the cavity function and its first derivative at $r = 0, 1$, and 2 . By eliminating the parameter ξ' in favor of $y(1)$ as $\xi' = \rho x y(1)$ one gets

$$y(0) = y(1) e^{\rho x y(1)} [1 - \rho x (1-x) y(1)], \quad (4.7)$$

$$\left. \frac{\partial \ln y(r)}{\partial r} \right|_{r=0} = - \frac{\rho x^2 y(1)}{1 - \rho x (1-x) y(1)}, \quad (4.8)$$

$$y'(2^+) - y'(2^-) = \rho x^2 [y(1)]^2. \quad (4.9)$$

Equations (4.7) and (4.8) can be considered as (approximate) extensions to finite temperatures ($x \neq 1$) of the zero separation theorems (2.69) and (2.67), respectively. Equation (4.9) gives the discontinuity of the slope of $g(r)$ at $r = 2$. It is interesting to note that, although Eq. (4.9) has been derived from our LT approximation, it is not only exact in the limit $x \rightarrow 1$, but also in the opposite limit $x \rightarrow 0$ (at $\rho x = \text{const}$), as can be verified by comparison with Eq. (2.36).

B. Temperature expansion

While the approximation (4.1) is expected to become more and more reliable as the temperature decreases, it is not restricted *a priori* to low temperatures since it incorporates all the orders in the parameter $\bar{x} \equiv 1 - x = e^{-1/T^*}$, i.e.,

$$\psi_n(r) = \psi_n^{(0)}(r) + \psi_n^{(1)}(r)\bar{x} + \psi_n^{(2)}(r)\bar{x}^2 + \dots \quad (4.10)$$

Let us now obtain explicitly $\psi_n^{(0)}(r)$ and $\psi_n^{(1)}(r)$. In the limit $\bar{x} \rightarrow 0$, the solution of Eq. (4.4) coincides with that of Eq. (2.54), namely $\xi = \xi_0 - \xi_0^2 e^{\xi_0} \bar{x} + \dots$ and $\xi' = \xi - \xi_0 e^{\xi_0} \bar{x} + \dots$, where ξ_0 is defined by Eq. (2.62). Therefore, from Eq. (2.60) we get

$$\psi_0^{(0)}(r) = 0, \quad \psi_n^{(0)}(r) = \frac{\xi_0^n}{\rho(n-1)!} e^{-\xi_0 r} r^{n-1}, \quad n \geq 1, \quad (4.11)$$

$$\psi_n^{(1)}(r) = \frac{\xi_0^{n+1}}{\rho^2 n!} e^{-\xi_0(r-1)} r^{n-1} [\xi_0(n+1-\rho)r - n^2]. \quad (4.12)$$

From $\psi_0^{(1)}(r)$ and $\psi_n^{(0)}(r)$ for $n \geq 1$, and taking into account that Eq. (4.5) yields $A = \xi_0^2 e^{\xi_0} \bar{x}^2 / \rho + \dots \sim \bar{x}^2$, one recovers the exact hard-rod result (2.65).

C. Density expansion

In the low density regime, the solution of Eq. (4.4) is

$$\xi = \rho (1 + x\rho + x^3 \rho^2) + \mathcal{O}(\rho^4), \quad (4.13)$$

$$\xi' = x\rho (1 + x^2 \rho) + \mathcal{O}(\rho^3). \quad (4.14)$$

Insertion into Eq. (4.5) yields

$$A = x(1-x)^2 \rho + \mathcal{O}(\rho^2). \quad (4.15)$$

The density expansion of the functions $\psi_n(r)$ defined by Eq. (2.60) is

$$\psi_0(r) = (1-x) [1 + x\rho(1+x-r)] + \mathcal{O}(\rho^2), \quad (4.16)$$

$$\psi_1(r) = x [1 + \rho(x^2 + r - 2xr)] + \mathcal{O}(\rho^2), \quad (4.17)$$

$$\psi_2(r) = x^2 \rho r + \mathcal{O}(\rho^2), \quad (4.18)$$

$$\psi_n(r) = \mathcal{O}(\rho^{n-1}), \quad n \geq 3. \quad (4.19)$$

Using (4.15)–(4.18) in the LT approximation (4.1) one recovers the exact result $y(r) = 1 + \rho y_1(r) + \mathcal{O}(\rho^2)$, where $y_1(r)$ is shown in Table II. Note that the inclusion of the term in Eq. (4.1) headed by the parameter A is essential to get this result. However, Eq. (4.1) does not reproduce the exact $y_2(r)$ for $r < 2$, except, of course, at $x = 1$.

D. Test for a very low temperature

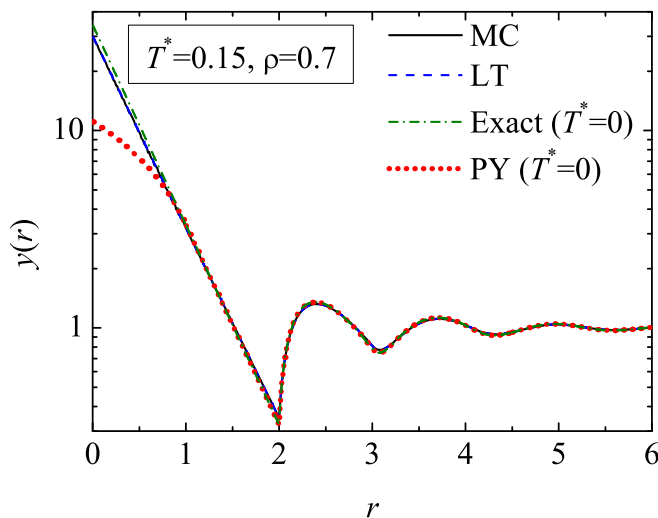


FIG. 5: (Color online) Plot of the cavity function $y(r)$ at $\rho = 0.7$ and $T^* = 0.15$. The solid line corresponds to MC simulations and the dashed line (which is practically indistinguishable from the solid line) represents the low-temperature (LT) approximation (4.1). The figure also includes the exact (dashed-dotted line) and the PY (dotted line) cavity functions at zero temperature.

As a test of the reliability of the LT approximation (4.1) for very low temperatures, we present in Fig. 5 a comparison with MC simulations at $\rho = 0.7$ and $T^* = 0.15$. The agreement is excellent. In fact, the simulation data cannot be distinguished from the theoretical results. While the temperature $T^* = 0.15$ is very low ($\bar{x} = 1 - x \simeq 1.3 \times 10^{-3}$), one can observe that $y(r)$ in the region $r < 1$ is slightly smaller than the one at $T^* = 0$. As in Fig. 3, Fig. 5 shows the failure of the PY approximation to account reasonably well for the cavity function inside the core. As a bonus, Fig. 5 illustrates that MC simulations of $g(r)$ for penetrable spheres at low temperatures (say $T^* \lesssim 0.2$) can be used to get (by extrapolation) the cavity function of *hard spheres* inside the core. This quantity is accessible from simulations of true hard spheres by an alternative method.⁴²

V. COMPARISON OF MONTE CARLO SIMULATIONS WITH THEORETICAL APPROXIMATIONS

As Figs. 4 and 5 illustrate, the HT approximation (3.5) and the LT approximation (4.1) become very accurate in their expected domains of sufficiently high and low temperatures, respectively. However, the physically most interesting cases correspond to moderate temperatures (say $0.5 \lesssim T^* \lesssim 2$), where the finite penetrability of the particles plays a relevant role. Now some interesting questions are as follows: Up to what temperature the

LT approximation remains reasonably accurate? Below which temperature the HT approximation ceases to be reliable? Do the answers to those questions depend on the density? To address these points we have performed MC simulations of the system⁴³ for four temperatures ($T^* = 0.3, 0.8, 1.5$, and 3.0) and, in each case, for three densities which roughly correspond to $\rho x \simeq 0.3, 0.5$, and 0.7 , except for the highest temperature ($T^* = 3.0$), in which case we have taken $\rho x \simeq 0.5, 0.8$, and 1.1 .

Figure 6 shows the simulation data and the theoretical predictions of the radial distribution function $g(r)$ at temperature $T^* = 0.3$ and densities $\rho = 0.3, 0.5$, and 0.7 . Although this is a rather low temperature, overlapping effects start to be important, especially as the density increases. It is then remarkable that the LT approximation yields results that are indistinguishable from the simulation data. On the one hand, as one could have anticipated, the HT approximation does not capture the rich structural features that are present at this relatively small temperature. On the other hand, it is noteworthy that, even at a temperature as low as $T^* = 0.3$, the results provided by the HT approximation are not unphysical.

Next we consider in Fig. 7 the moderate temperature $T^* = 0.8$ and the densities $\rho = 0.4, 0.7$, and 1 . The LT approximation still yields excellent results, although it tends to slightly underestimate $g(r)$ near contact and in the overlapping region as density increases. The HT approximation is reasonable at a qualitative level only.

The temperature $T^* = 1.5$ is a representative example of a transitional value, as illustrated in Fig. 8 for $\rho = 0.6, 1$, and 1.4 . At the lowest density ($\rho = 0.6$) the LT theory is still quite good, the HT theory being only slightly less accurate. At the intermediate density ($\rho = 1$), both theories practically coincide and underestimate $g(r)$ near contact and in the overlapping region. Finally, at the highest density ($\rho = 1.4$), the preferable theory is the HT one, except for $r \gtrsim 1.5$. Thus, although the temperature is the most important parameter to determine which approximation is better, the density can also play a relevant role.

Figure 9 shows $g(r)$ at a higher temperature $T^* = 3$ and for the densities $\rho = 1.7, 2.8$, and 3.9 . Now the HT approximation succeeds in reproducing the simulation data quite well for the three densities, while the LT approximation becomes rather poor, especially as the density increases.

It is interesting to note from the simulation curves in Figs. 6–9 that the curvature of $g(r)$ in the shell $1 < r < 2$ changes from concave to convex as the temperature increases. Moreover, at a given temperature, the magnitude of the curvature increases with the density. We also observe that, as temperature and density increase, so does the number of overlapped pairs. Nevertheless, the radial distribution function in the non-overlapping region ($r > 1$) becomes less structured as temperature increases.

The comparison between MC data and the LT and HT

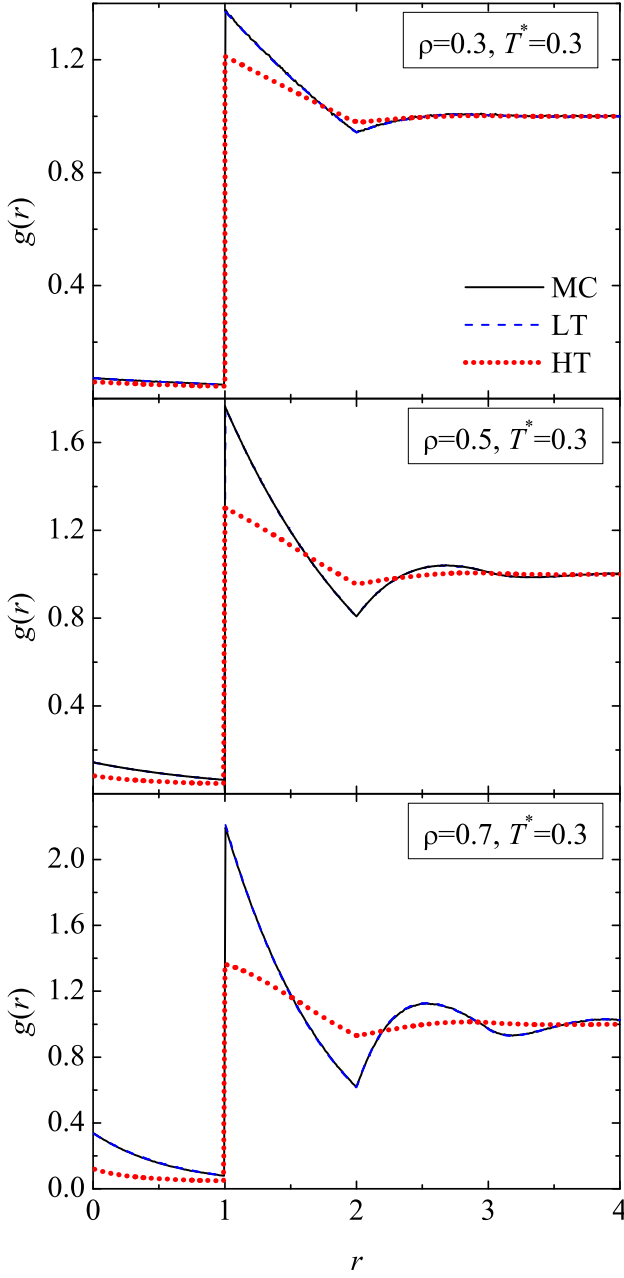


FIG. 6: (Color online) Plot of the radial distribution function $g(r)$ at $T^* = 0.3$ and $\rho = 0.3$ (top panel), $\rho = 0.5$ (middle panel), and $\rho = 0.7$ (bottom panel). The solid lines correspond to MC simulations, the dashed lines (which are practically indistinguishable from the solid lines) represent the low-temperature (LT) approximation (4.1), and the dotted lines represent the high-temperature (HT) approximation (3.5).

theories carried out in Figs. 6–9 shows that both theories keep being reasonably accurate well beyond their respective expected domains. In general, the smaller the temperature and/or the density, the better the LT theory, while the opposite happens for the HT theory. Both theories complement each other so well that they meet and become practically equivalent for intermediate tempera-

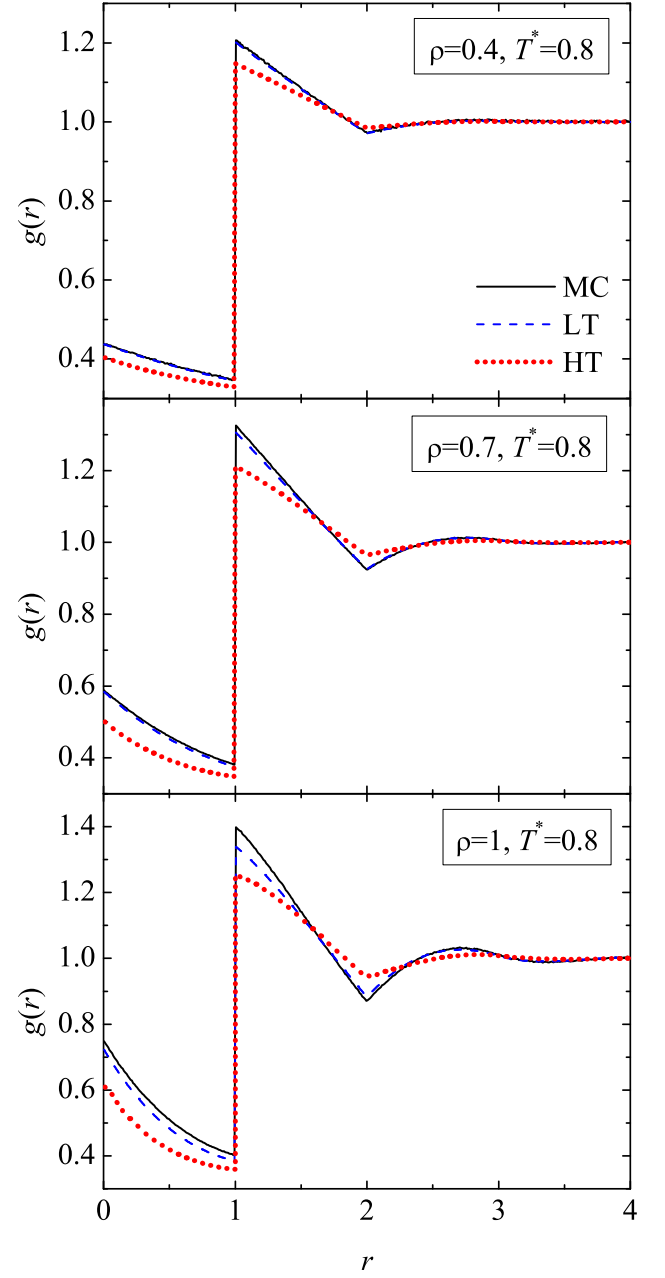


FIG. 7: (Color online) Plot of the radial distribution function $g(r)$ at $T^* = 0.8$ and $\rho = 0.4$ (top panel), $\rho = 0.7$ (middle panel), and $\rho = 1$ (bottom panel). The solid lines correspond to MC simulations, the dashed lines (which are practically indistinguishable from the solid lines in the top and middle panels) represent the low-temperature (LT) approximation (4.1), and the dotted lines represent the high-temperature (HT) approximation (3.5).

tures and densities, as illustrated by the middle panel of Fig. 8. In order to define the “basins” of both theories in the density-temperature plane, let us consider the locus of points $\tilde{\rho}(T^*)$ where the contact quantity $y(1) = g(1^+)$ takes the same value in both approximations. This locus is plotted in Fig. 10 in the representation ρx vs T^* . We

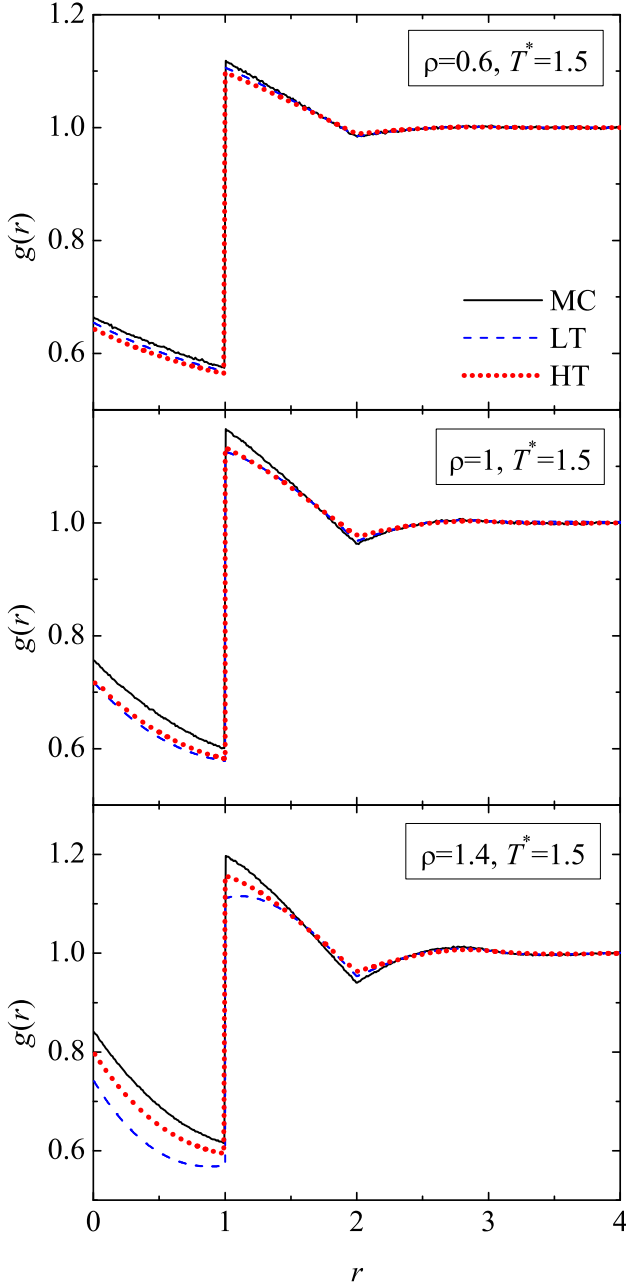


FIG. 8: (Color online) Plot of the radial distribution function $g(r)$ at $T^* = 1.5$ and $\rho = 0.6$ (top panel), $\rho = 1$ (middle panel), and $\rho = 1.4$ (bottom panel). The solid lines correspond to MC simulations, the dashed lines represent the low-temperature (LT) approximation (4.1), and the dotted lines represent the high-temperature (HT) approximation (3.5). Note that the dashed and dashed-dotted lines in the middle panel are hardly distinguishable.

have used the scaled density ρx rather than the true density ρ because the range of values of ρ accessible to the fluid phase increases with increasing temperature roughly as $\rho \sim 1/x$.¹⁸ From Fig. 10 and the comparison with MC results carried out in Figs. 4–9 one can conclude that the LT approximation is reliable for $T^* \lesssim 0.8$ at any den-

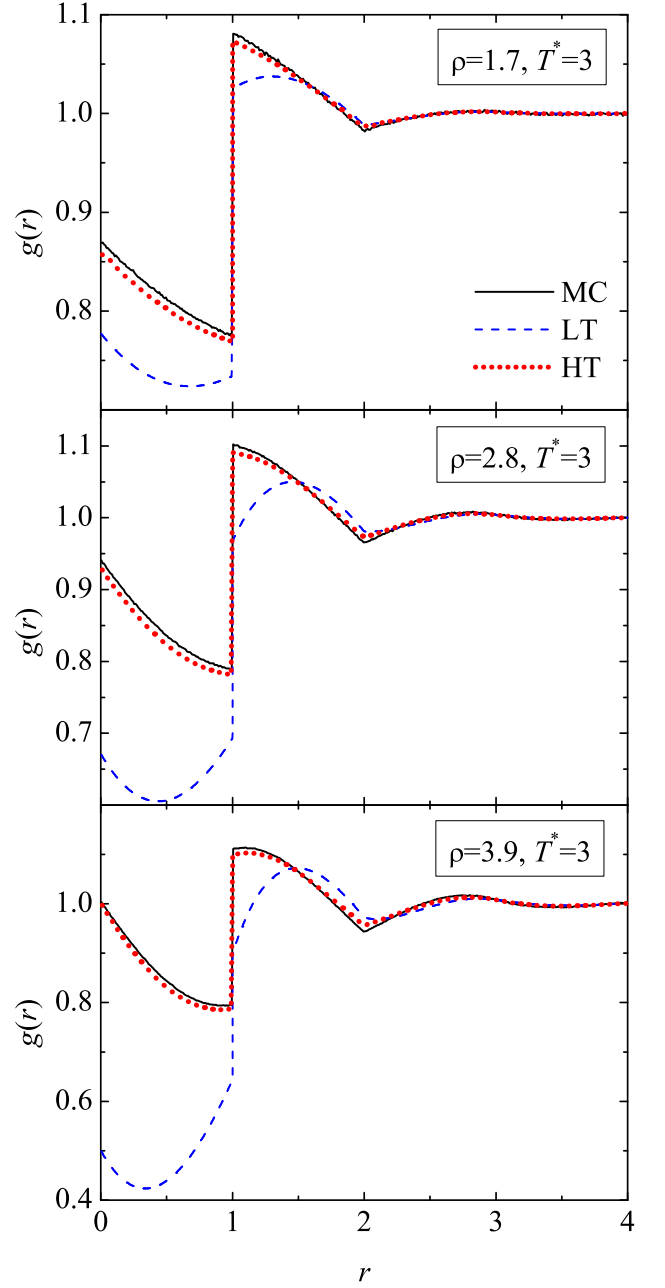


FIG. 9: (Color online) Plot of the radial distribution function $g(r)$ at $T^* = 3$ and $\rho = 1.7$ (top panel), $\rho = 2.8$ (middle panel), and $\rho = 3.9$ (bottom panel). The solid lines correspond to MC simulations, the dashed lines represent the low-temperature (LT) approximation (4.1), and the dotted lines represent the high-temperature (HT) approximation (3.5).

sity, while the HT approximation is reliable for $T^* \gtrsim 3$ at any density. Between these two temperatures the locus defined by the condition $y_{\text{LT}}(1) = y_{\text{HT}}(1)$ separates the basins of each approximation. In that transitional regime, the smaller (larger) the density the better the LT (HT) theory is. For states lying on the locus both approximations yield practically equivalent predictions,

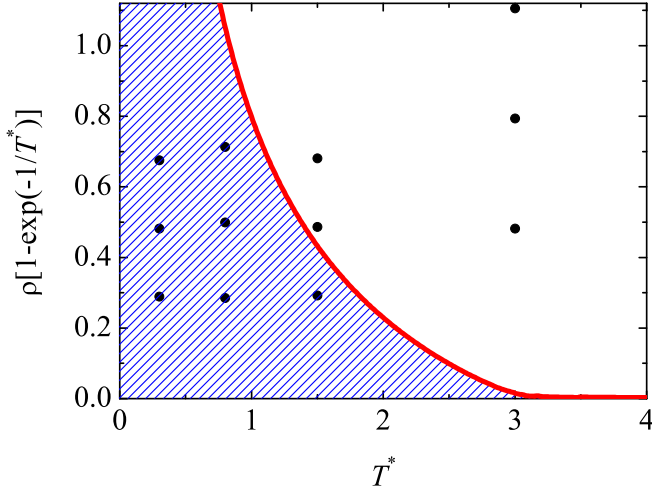


FIG. 10: (Color online) The thick solid line represents the locus of points in the plane ρx vs T^* where the LT and HT approximations predict the same value of the contact quantity $y(1) = g(1^+)$. The LT approximation is accurate below the curve (shaded region), while the HT approximation is accurate above the curve. The circles represent the states considered in Figs. 6–9.

which slightly underestimate $g(r)$ for distances $r \lesssim 1.5$ (cf. Fig. 8). As one departs from the locus, the quality of the corresponding approximation (either LT or HT) significantly improves, as illustrated by Figs. 5–7 in the LT case, and by Figs. 4 and 9 in the HT case. A global approximation can be proposed just by adopting either the LT or the HT approximation, depending on which basin the state point lies in. More specifically,

$$g(r; \rho, T^*) = \Theta(\alpha(\rho, T^*))g_{\text{LT}}(r; \rho, T^*) + \Theta(-\alpha(\rho, T^*))g_{\text{HT}}(r; \rho, T^*), \quad (5.1)$$

where

$$\alpha(\rho, T^*) = y_{\text{LT}}(1; \rho, T^*) - y_{\text{HT}}(1; \rho, T^*). \quad (5.2)$$

While we have been concerned in this paper with heuristic *analytical* approximations, it is worthwhile comparing our MC data with the two classical integral equation theories. For one-dimensional systems, the PY and HNC integral equations read

$$y(r) = 1 + \rho \int_{-\infty}^{\infty} ds h(|s|) y(|r-s|) f(|r-s|), \quad (5.3)$$

$$\ln y(r) = \rho \int_{-\infty}^{\infty} ds h(|s|) [h(|r-s|) - \ln y(|r-s|)], \quad (5.4)$$

respectively, where we recall that $h(r) = e^{-\varphi(r)/k_B T} y(r) - 1$. We have numerically solved the above two equations by a standard iterative method for the simulated states. The agreement is always quite good outside the core ($r > 1$), so that we focus now

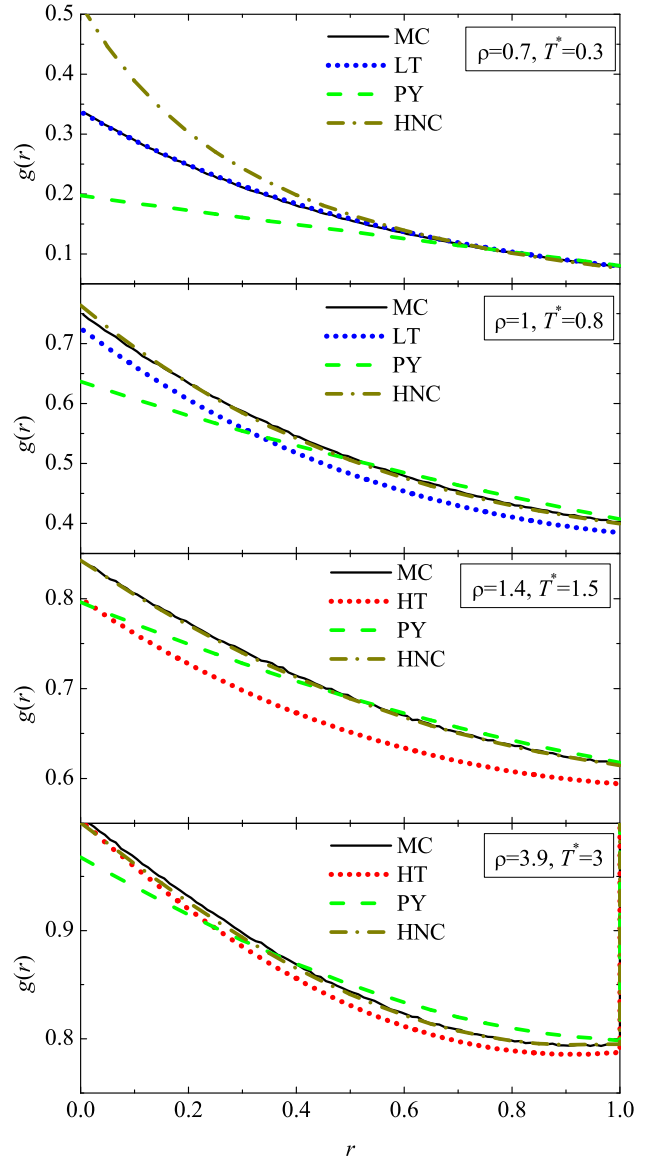


FIG. 11: (Color online) Radial distribution function inside the core at four different states, as obtained from MC simulations (solid lines), the LT or HT approximations (dotted lines), the PY theory (dashed lines), and the HNC theory (dashed-dotted lines). Note that the LT results are indistinguishable from the MC data in the top panel, while the HNC results are hardly distinguishable from the MC data in the remaining three panels.

on the overlapping region. Figure 11 shows $g(r)$ with $r < 1$ for the temperatures $T^* = 0.3, 0.8, 1.5$, and 3 , and, in each case, for the highest density considered in the simulations. Apart from the simulation data and the PY and HNC predictions, we have also included either our LT approximation ($T^* = 0.3$ and 0.8) or our HT approximation ($T^* = 1.5$ and 3), in accordance with Fig. 10. At the lowest temperature ($T^* = 0.3$) the PY and HNC predictions seriously underestimate and overestimate, respectively, the simulation data,

while the LT approximation is excellent. However, at moderate and high temperatures ($T^* = 0.8, 1.5$, and 3) the HNC approximation becomes very good. The PY approximation is still worse than our LT approximation at $T^* = 0.8$ but is more accurate than our HT approximation at $T^* = 1.5$. At $T^* = 3$, the PY and HT approximations exhibit a comparable accuracy. Note that as temperature increases, the HT, PY, and HNC approximations tend to coincide and reduce to the exact asymptotic behavior (2.21). The good performance of the HNC approximation at moderate temperatures reported here contrasts with the situation reported in the three-dimensional case.^{13,14}

VI. SUMMARY AND DISCUSSION

It is obvious that many of the physical properties of real 3D systems cannot be fully represented by 1D models. For instance, entropy-driven phase transitions, such as the fluid-solid transition in hard spheres or the demixing transition in positively nonadditive hard-sphere mixtures, are absent in 1D. In the case of penetrable spheres, however, the 1D model retains a number of features of its 2D and 3D counterparts (such as the lack of an exact solution, the formation of “clumps” of overlapped particles,¹⁰ or the existence of a fluid-solid phase transition,¹⁸) what justifies its study, apart from its interest at a more fundamental level.

In this paper we have investigated the structural properties of one-dimensional fluids of penetrable spheres. First we have derived the exact expression of the radial distribution function $g(r)$ through second order in density at any temperature, the results being presented in Table II. This calculation already reveals some of the main features of the PY and HNC approximations: the former underestimates $g(r)$ inside the core ($r < 1$), while the latter overestimate it. Moreover, the HNC predictions become better than the PY ones for temperatures larger than $T^* \approx 1$.

In the limit of asymptotically high temperatures only the linear chain diagrams contributing to the virial expansion of the cavity function need to be retained. The series can then be resummed, the result being given by Eqs. (2.21) and (2.27). The auxiliary function $w(r)$, which depends on density and temperature only through the scaled quantity ρx , where x is defined by Eq. (2.9), embodies the structural properties of the high-temperature penetrable-rod fluid. Its series in powers of ρx converges uniformly for $\rho x < \frac{1}{2}$, so that this is the radius of convergence of the virial series of the equation of state. An explicit representation of $w(r)$ for each shell $n < r < n + 1$ has been derived, Eq. (2.32), what has allowed us to get some simple relations, Eqs. (2.35)–(2.40).

The high-temperature limit has been complemented by the zero-temperature limit. In that limit the system becomes a hard-rod fluid, whose expression for $g(r)$ is known exactly. Since the particles are impenetrable in

this limit, $g(r)$ vanishes for $r < 1$. However, the cavity function $y(r)$ remains finite and its determination is important to understand the behavior of $g(r)$ for low (but non-zero) temperatures. In order to derive $y(r)$ for hard rods, we have first applied to finite temperatures the scheme providing the exact solution in the case of interactions restricted to nearest neighbors. Although the penetrable-rod potential at non-zero temperature allows for multiple interactions, the nearest-neighbor approximation becomes more and more reliable as the temperature decreases, providing thus the exact $y(r)$ for $r < 1$ in the hard-rod limit. We are not aware of any previous derivation of $y(r)$ for hard rods inside the core, although it might possibly exist. Quite surprisingly, the expression of $y(r)$ for $r < 1$ is just the analytical continuation of its expression for $1 < r < 2$, so that the hard-rod cavity function is fully analytical at $r = 1$, even though the potential is highly singular at that point. It is well known that the PY approximation gives the exact $g(r)$ for hard rods due a fortunate mutual cancelation of the neglected diagrams in the region $r > 1$. However, it is perhaps less known²⁵ that such a cancelation does not take place for $r < 1$, what results in a wrong PY prediction of $y(r)$ inside the core, already to second order in density. In fact, the PY and HNC cavity functions for hard rods exhibit an artificial second-order discontinuity at $r = 1$. The failure of the PY theory to reproduce the hard-rod $y(r)$ inside the core is a precursor of its tendency to dramatically underestimate the penetrability phenomenon at finite temperatures.

It seems tempting to exploit the exact asymptotic behavior of the correlation functions for high temperatures by extrapolating it to finite temperatures. Among several possibilities, we have taken the Padé approximant (3.5) as our high-temperature (HT) approximation. It is equivalent to retaining, in addition to all the linear chain diagrams, all the reducible diagrams factorizing into linear chain diagrams, although those reducible diagrams have enhanced factors that partially compensate for the neglected irreducible diagrams. In addition, while $x \approx 1/T^*$ for high temperatures, we have kept the non-linear relationship (2.9) in the extension to finite temperatures since this is the parameter naturally appearing in the virial expansion. Despite its simplicity, we have checked by comparison with MC simulations that this HT approximation does quite a good job for temperatures higher than $T^* \approx 3$ at any density.

Obviously, the HT approximation is not accurate for low temperatures. To complement it we have constructed a low-temperature (LT) approximation, which is based on the explicit expression for $g(r)$ obtained from the nearest-neighbor approximation mentioned above but introduces two changes. First, the transcendental equation that the damping coefficient ξ obeys in the nearest-neighbor approximation is replaced by another one coming from the continuity condition of $y(r)$ at $r = 1$. Next, a linear function is added in the region $r < 1$ to enforce continuity of the first derivative of $y(r)$ at $r = 1$.

More specifically, in the LT approximation $g(r)$ is given by Eq. (4.1), where the functions $\psi_n(r)$ are defined by Eq. (2.60) and the amplitude A is given by Eq. (4.5); in those equations, the parameter ξ' is defined by Eq. (2.55) and finally the parameter ξ is the solution to the transcendental equation (4.4). This LT approximation reduces to the exact solution in the hard-rod limit. In addition, it is excellent for low temperatures (e.g., $T^* = 0.3$) and quite good up to $T^* \approx 0.8$ at any density.

For intermediate temperatures ($0.8 \lesssim T^* \lesssim 3$), the LT and HT theories compete each other, the former being better for densities lower than a certain threshold value $\tilde{\rho}(T^*)$ and the latter being better for $\rho > \tilde{\rho}(T^*)$. In fact, both theories yield almost identical predictions for states lying on the curve $\tilde{\rho}(T^*)$. As one departs from that curve by decreasing (increasing) the density and/or temperature the quality of the LT (HT) approximation improves significantly. Therefore, given the simplicity and analytic character of both approximations, it is quite reinforcing that they match and complement so well that their combined use [cf. Eqs. (5.1) and (5.2)] covers satisfactorily the whole range of densities and temperatures. Of course, it would be much nicer to have a unique analytic approximation being equally accurate for both low and high temperatures. However, we have not been able to devise such a unique approach.

To put these results in a proper perspective, we have also compared our MC data with numerical solutions of the PY and HNC integral equations. The results show that the PY approximation is quite poor at low temperatures, slowly improving as the temperature increases. The HNC approximation, on the other hand, is inaccurate only at low temperatures, being excellent at moderate and high temperatures ($T^* \gtrsim 0.8$).

Although restricted to one-dimensional systems, the research carried out in this paper can be used to pave the way to similar approaches in the more realistic case of three-dimensional penetrable-sphere fluids. Since the asymptotic high-temperature behavior is given by Eqs. (2.21) and (2.22) for any dimensionality,¹⁸ the proposal of the HT approximation is straightforward. The only difference is that now the (three-dimensional) Fourier transform of the auxiliary function $w(r)$ is given by

$$\tilde{w}(k) = 96\pi\eta x \frac{(k \cos k - \sin k)^2}{k^3 [k^3 - 24\eta x (k \cos k - \sin k)]}, \quad (6.1)$$

where $\eta = (\pi/6)\rho$ is the packing fraction. The construction of the LT approximation is less direct since the exact solution in the hard-sphere limit is not known. However, we can use the analytic solution of the PY equation for hard spheres^{26,27,44} as a starting point. The structure of the resulting proposal is

$$g(r) = \hat{g}(r) \exp\{(r-1)[A + Br(r+1)]\Theta(1-r)\}, \quad (6.2)$$

where the Laplace transform of $r\hat{g}(r)$ is

$$\hat{G}(t) = \frac{t}{12\eta} \frac{P(t)}{1 + P(t)}, \quad P(t) = \frac{L_0 - e^{-t}(L_0 + 1 + L_1 t)}{1 + S_1 t + S_2 t^2 + S_3 t^3}. \quad (6.3)$$

In Eqs. (6.2) and (6.3), the coefficients A , B , L_i , and S_i are functions of η and T^* determined by imposing consistency conditions. In the limit $T^* \rightarrow 0$ the coefficients A , B , and L_0 vanish and one recovers the radial distribution function for hard spheres in the PY approximation. However, the cavity function $y(r)$ in the region $r < 1$ differs from the PY one even in that limit, in parallel to what happens in the 1D case. Preliminary comparisons of the HT and LT approximations (6.1) and (6.2) with MC simulations are quite encouraging. A detailed report will be published elsewhere.⁴⁵

Acknowledgments

One of the authors (A.M.) is grateful to the hospitality of the University of Extremadura and its Social Council during a stay in May and June 2004, when this work was started. His research has been partially supported by the Ministry of Education, Youth, and Sports of the Czech Republic under the project No. LC 512. The research of the other author (A.S.) has been supported by the Ministerio de Educación y Ciencia (Spain) through Grant No. FIS2004-01399 (partially financed by FEDER funds) and by the European Community's Human Potential Programme under contract No. HPRN-CT-2002-00307, DYGLAGEMEM.

APPENDIX: DERIVATION OF EQUATIONS (2.29), (2.30), AND (2.32)

Expanding (2.22) in powers of density, one gets (2.28) with

$$\begin{aligned} w_n(r) &= \frac{1}{2\pi} \int_{-\infty}^{\infty} dk e^{ikr} [\tilde{f}_{\text{HS}}(k)]^n \\ &= \frac{1}{2\pi} \int_{-\infty}^{\infty} dk e^{ikr} \left(-\frac{2 \sin k}{k} \right)^n \\ &= \frac{i^n}{2\pi} \sum_{m=0}^n \binom{n}{m} (-1)^{n+m} \int_L dk \frac{e^{ik(r+2m-n)}}{k^n}, \end{aligned} \quad (A.1)$$

where L is a path in the complex plane from $k = -\infty$ to $k = +\infty$ that goes round the singularity at $k = 0$ from above. If $r + 2m - n > 0$, we can close the path with an upper half circle of infinite radius, so that the integral identically vanishes. If $r + 2m - n < 0$ we close the path with a lower half circle, so that the contour encircles a pole at $k = 0$ of order n . By applying the residue theorem, we then have

$$\begin{aligned} \int_L dk \frac{e^{ik(r+2m-n)}}{k^n} &= \frac{2\pi}{(n-1)!} (-i)^n (n-2m-r)^{n-1} \\ &\quad \times \Theta(n-2m-r). \end{aligned} \quad (A.2)$$

Inserting this into Eq. (A.1) one gets Eq. (2.29).

Let us now prove Eq. (2.30). First, we note that, by symmetry,

$$\frac{1}{2\pi i} \int_{-\infty}^{\infty} dk \frac{(-2 \sin k)^{n+1}}{k^n} = 0. \quad (\text{A.3})$$

By following on the left-hand side steps similar to those followed to derive Eqs. (A.1) and (A.2), we get the identity (for $n \geq 2$)

$$0 = \sum_{m=0}^{[(n+1)/2]} \frac{(-1)^{n+m+1}}{m!(n+1-m)!} (n+1-2m)^{n-1}, \quad (\text{A.4})$$

where $[a]$ denotes the integer part of a . Next, setting $r = 1$ in Eq. (2.29) and making the change $m \rightarrow m+1$, we have

$$\frac{w_n(1)}{n} = \sum_{m=0}^{[(n+1)/2]} \frac{(-1)^{n+m+1} m}{m!(n+1-m)!} (n+1-2m)^{n-1}. \quad (\text{A.5})$$

Therefore,

$$\begin{aligned} \frac{w_{n+1}(0)}{n+1} + 2 \frac{w_n(1)}{n} &= (n+1) \sum_{m=0}^{[(n+1)/2]} \frac{(-1)^{n+m+1}}{m!(n+1-m)!} \\ &\quad \times (n+1-2m)^{n-1}. \end{aligned} \quad (\text{A.6})$$

On account of Eq. (A.4), the right-hand side of Eq. (A.6) vanishes, what proves Eq. (2.30).

Finally, we want to collect together all the terms contributing to the same Heaviside function in Eq. (2.28). We first define the index $p = 2m - n$ and note that if $p = 1$ then $n = 1 + 2q$ and $m = 1 + q$ with $q = 1, 2, 3, \dots$, while if $p \geq 2$ then $n = p + 2q$ and $m = p + q$ with $q = 0, 1, 2, \dots$. Therefore,

$$\begin{aligned} w(r) &= \sum_{q=1}^{\infty} \frac{(-1)^{1+q}(1+2q)}{(1+q)!q!} (\rho x)^{2q} (1-r)^{2q} \Theta(1-r) \\ &\quad + \sum_{p=2}^{\infty} \sum_{q=0}^{\infty} \frac{(-1)^{p+q}(p+2q)}{(p+q)!q!} (\rho x)^{p+2q-1} (p-r)^{p+2q-1} \\ &\quad \times \Theta(p-r). \end{aligned} \quad (\text{A.7})$$

Making use of the identity³⁴

$$\sum_{q=0}^{\infty} \frac{(-1)^q (p+2q)}{(p+q)!q!} z^{p+2q-1} = 2J'_p(2z), \quad (\text{A.8})$$

where $J'_p = \frac{1}{2}(J_{p-1} - J_{p+1})$ is the first derivative of the Bessel function of the first kind J_p , Eq. (A.7) reduces to Eq. (2.32).

* Electronic address: amail@post.cz

† Electronic address: andres@unex.es;
URL: <http://www.unex.es/eweb/fisteor/andres/>

- ¹ C. N. Likos, Phys. Rep. **348**, 267 (2001), and references therein.
- ² C. N. Likos, H. Löwen, M. Watzlawek, B. Abbas, O. Jucknischke, J. Allgaier, and D. Richter, Phys. Rev. Lett. **80**, 4450 (1998); M. Watzlawek, C. N. Likos, and H. Löwen, *ibid.* **82**, 5289 (1999).
- ³ F. H. Stillinger and D. K. Stillinger, Physica A **244**, 358 (1997).
- ⁴ H. Graf and H. Löwen, Phys. Rev. E **57**, 5744 (1998).
- ⁵ A. Lang, C. N. Likos, M. Watzlawek, and H. Löwen, J. Phys.: Condens. Matter **12**, 5087 (2000).
- ⁶ A. A. Louis, P. G. Bolhuis, and J.-P. Hansen, Phys. Rev. E **62**, 7961 (2000).
- ⁷ C. N. Likos, A. Lang, M. Watzlawek, and H. Löwen, Phys. Rev. E **63**, 031206 (2001).
- ⁸ R. Finken, J.-P. Hansen, and A. A. Louis, J. Stat. Phys. **110**, 1015 (2003).
- ⁹ C. Marquest and T. A. Witten, J. Phys. (France) **50**, 1267 (1989).
- ¹⁰ W. Klein, H. Gould, R. A. Ramos, I. Clejan, and A. I. Mel'cuk, Physica A **205**, 738 (1994).
- ¹¹ C. N. Likos, M. Watzlawek, and H. Löwen, Phys. Rev. E **58**, 3135 (1998).
- ¹² M. Schmidt, J. Phys.: Condens. Matter **11**, 10163 (1999).
- ¹³ M. J. Feraud, E. Lomba, and L. L. Lee, J. Chem. Phys. **112**, 810 (2000).
- ¹⁴ Y. Rosenfeld, M. Schmidt, M. Watzlawek, and H. Löwen,

- Phys. Rev. E **62**, 5006 (2000).
- ¹⁵ M. Schmidt and M. Fuchs, J. Chem. Phys. **117**, 6308 (2002).
- ¹⁶ S.-C. Kim and S.-Y. Suh, J. Chem. Phys. **117**, 9880 (2002).
- ¹⁷ N. Choudhury and S. K. Ghosh, J. Chem. Phys. **119**, 4827 (2003).
- ¹⁸ L. Acedo and A. Santos, Phys. Lett. A **323**, 427 (2004).
- ¹⁹ A. Santos, "Kinetic Theory of Soft Matter. The Penetrable-Sphere Model," in *Rarefied Gas Dynamics: 24th International Symposium on Rarefied Gas Dynamics*, edited by M. Capitelli (AIP Conference Proceedings **762**, 2005), pp. 276–281; cond-mat/0501068.
- ²⁰ L. Groome, J. W. Dufty, and M. J. Lindenfeld, Phys. Rev. A **19**, 304 (1979).
- ²¹ J. A. Cuesta and A. Sánchez, J. Phys. A: Math. Gen. **35**, 2373 (2002); J. Stat. Phys. **115**, 869 (2004).
- ²² D. C. Mattis, *The Many-Body Problem: An Encyclopedia of Exactly Solved Models in One Dimension* (World Scientific, Singapore, 1993).
- ²³ See, for instance, G. Jannink and J. des Cloizeaux, J. Phys.: Condens. Matter **2**, 1 (1990); J. des Cloizeaux and G. Jannink, *Polymers in Solution: Their Modelling and Structure* (Clarendon Press, Oxford, 1991).
- ²⁴ L. Verlet, Physica **30**, 95 (1964).
- ²⁵ A. Münster, *Statistical Thermodynamics*, vol. 1 (Springer-Verlag, Berlin, 1969), Chap. 5.11.
- ²⁶ R. Balescu, *Equilibrium and Nonequilibrium Statistical Mechanics* (Wiley, New York, 1974).
- ²⁷ J.-P. Hansen and I. R. McDonald, *Theory of Simple Liquids*, (Academic Press, London, 1986).

- ²⁸ J. A. Barker and D. Henderson, *Rev. Mod. Phys.* **48**, 587 (1976).
- ²⁹ A. Santos, *J. Chem. Phys.* **123**, 104102 (2005).
- ³⁰ D. J. Gates, *Physica A* **81**, 47 (1975).
- ³¹ N. Grewe and W. Klein, *J. Math. Phys.* **18**, 1729, 1735 (1977).
- ³² W. Klein and N. Grewe, *J. Chem. Phys.* **72**, 5456 (1980).
- ³³ W. Klein and A. C. Brown, *J. Chem. Phys.* **78**, 6960 (1981).
- ³⁴ *Handbook of Mathematical Functions*, edited by M. Abramowitz and I. A. Stegun (Dover, New York, 1972).
- ³⁵ Z. W. Salsburg, R. W. Zwanzig, and J. G. Kirkwood, *J. Chem. Phys.* **21**, 1098 (1953).
- ³⁶ I. Prigogine and S. Lafleur, *Bull. Classe Sci. Acad. Roy. Bel.* **263**, 484, 497 (1954).
- ³⁷ R. Kikuchi, *J. Chem. Phys.* **23**, 2327 (1955).
- ³⁸ J. Lebowitz and D. Zomick, *J. Chem. Phys.* **54**, 3335 (1971).
- ³⁹ M. Heying and D. Corti, *Fluid Phase Equil.* **220**, 85 (2004).
- ⁴⁰ G. Stell, *Physica* **29**, 517 (1963).
- ⁴¹ L. L. Lee, *J. Chem. Phys.* **103**, 9388 (1995); L. L. Lee, D. Ghonasgi, and E. Lomba, *ibid.* **104**, 8058 (1996); L. L. Lee and A. Malijevský, *ibid.* **114**, 7109 (2001).
- ⁴² S. Labík and A. Malijevský, *Mol. Phys.* **53**, 381 (1984).
- ⁴³ We have employed the conventional Metropolis algorithm on an NVT ensemble with periodic boundary conditions. Typically, $N = 10^4$ particles are used. In each realization, the correlation functions are measured every 100 MC sweeps and this cycle is repeated 2×10^4 times. The time-averaged quantities are further averaged over ten independent realizations.
- ⁴⁴ M. S. Wertheim, *Phys. Rev. Lett.* **10**, 321 (1963); E. Thiele, *J. Chem. Phys.* **39**, 474 (1963).
- ⁴⁵ Al. Malijevský, S. B. Yuste, and A. Santos, unpublished.